

THE NORTHERN WRAPS OF THE SAGITTARIUS STREAM AS TRACED BY RED CLUMP STARS:  
 DISTANCES, INTRINSIC WIDTHS AND STELLAR DENSITIES.

M. CORRENTI

Universitá di Bologna, Dipartimento di Astronomia, via Ranzani 1, 40127, Bologna, Italy

M. BELLAZZINI

INAF - Osservatorio Astronomico di Bologna, via Ranzani 1, 40127, Bologna, Italy

R.A. IBATA

Observatoire Astronomique, Université de Strasbourg, CNRS, 11, rue de l'Université, F-67000 Strasbourg, France

F.R. FERRARO

Universitá di Bologna, Dipartimento di Astronomia, via Ranzani 1, 40127, Bologna, Italy

AND

A. VARGHESE

Observatoire Astronomique, Université de Strasbourg, CNRS, 11, rue de l'Université, F-67000 Strasbourg, France

*Submitted 07 April 2010, Received 19 April 2010, Accepted 18 July 2010*

ABSTRACT

We trace the tidal Stream of the Sagittarius dwarf spheroidal galaxy (Sgr dSph) using Red Clump stars from the catalog of the Sloan Digital Sky Survey - Data Release 6, in the range  $150^\circ \lesssim RA \lesssim 220^\circ$ , corresponding to the range of orbital azimuth  $220^\circ \lesssim \Lambda \lesssim 290^\circ$ . Substructures along the line of sight are identified as significant peaks in the differential star count profiles (SCP) of candidate Red Clump stars. A proper modeling of the SCPs allows us to obtain: (a)  $\lesssim 10\%$  accurate, purely differential distances with respect to the main body of Sgr, (b) estimates of the FWHM along the line of sight, and (c) estimates of the local density, for each detected substructure. In the range  $255^\circ \lesssim \Lambda \lesssim 290^\circ$  we cleanly and continuously trace various coherent structures that can be ascribed to the Stream, in particular: the well known northern portion of the leading arm, running from  $d \simeq 43$  kpc at  $\Lambda \simeq 290^\circ$  to  $d \simeq 30$  kpc at  $\Lambda \simeq 255^\circ$ , and a more nearby coherent series of detections lying at constant distance  $d \simeq 25$  kpc, that can be identified with a wrap of the trailing arm. The latter structure, predicted by several models of the disruption of Sgr dSph, was never traced before; comparison with existing models indicates that the difference in distance between these portions of the leading and trailing arms may provide a powerful tool to discriminate between theoretical models assuming different shapes of the Galactic potential. A further, more distant wrap in the same portion of the sky is detected only along a couple of lines of sight. For  $\Lambda \lesssim 255^\circ$  the detected structures are more complex and less easily interpreted. We are confident to be able to trace the continuation of the leading arm down to  $\Lambda \simeq 220^\circ$  and  $d \simeq 20$  kpc; the trailing arm is seen up to  $\Lambda \simeq 240^\circ$  where it is replaced by more distant structures. Possible detections of more nearby wraps and of the Virgo Stellar Stream are also discussed. These measured properties provide a coherent set of observational constraints for the next generation of theoretical models of the disruption of Sgr.

*Subject headings:* galaxies: dwarf – Galaxy: structure – (galaxies:) Local Group – stars: distances – Galaxy: formation

1. INTRODUCTION

Stellar tidal streams as well as other substructures in the Milky Way (MW) halo are generally interpreted as the relics of the process of hierarchical formation of the MW, as envisaged by the currently accepted cosmological model ( $\Lambda$ -Cold Dark Matter,  $\Lambda$ -CDM hereafter, see Bullock et al. 2001; Madau et al. 2008, and references therein). With the advent of large modern surveys, like the 2 Micron All Sky Survey (2MASS, Skrutskie et al. 2006) and the Sloan Digital Sky Survey (SDSS, Adelman-McCarthy et al. 2008, and references therein), our ability to detect stellar systems and/or structures in the

halo and in the disk of the MW has increased dramatically and several large-scale likely relics of the build-up of the Galactic halo have been identified (Ibata et al. 2001a; Newberg et al. 2002; Yanny et al. 2003; Majewski et al. 2003; Martin et al. 2004; Belokurov et al. 2006; Jurić et al. 2008). Also smaller tidal streams have been found around disrupting globular clusters (see, for example Rockosi et al. 2002; Grillmair & Johnson 2006) or lacking an evident progenitor (Grillmair & Dionatos 2006; Belokurov et al. 2006, hereafter Bel06). The most spectacular example of the process of tidal disruption and accretion of a dwarf satellite into our Galaxy is the Sagittarius dwarf spheroidal galaxy (Sgr dSph), originally discovered by Ibata et al. (1994). The main body of the Sgr

galaxy is located at  $\sim 26$  kpc (Monaco et al. 2004) from the Sun, beyond the Galactic bulge (Galactic coordinates  $l, b = +5.6^\circ, -14.0^\circ$ ). The stellar content of the Sgr dSph is dominated by an intermediate-age relatively metal-rich population, with distributions peaking at age  $\sim 6$ -8 Gyr and  $[Fe/H] \sim -0.5$ , (see Bellazzini et al. 2006a, hereafter B06a, and references therein) but there is also clear evidence for the presence of an older ( $> 10$  Gyr) and more metal-poor population as well, including Blue Horizontal Branch (BHB, Ibata et al. 1997; Bellazzini et al. 1999a; Monaco et al. 2003) and RR Lyrae stars (Mateo et al. 1995a; Alcock et al. 1997; Cseresnjes 2001). All the available spectroscopic analyses indicate that the Metallicity Distribution (MD) of Sgr stars is characterized by a broad peak in the range  $-1.0 \lesssim [Fe/H] \lesssim 0.0$ , with a weak tail likely extending beyond  $[Fe/H] \lesssim -2.0$  (see B06a, Cseresnjes 2001; Monaco et al. 2005a; Mc William & Smecker-Hane 2006; Bonifacio et al. 2006; Sbordone et al. 2007; Bellazzini et al. 2008; Lagadec et al. 2009).

The body of Sgr dSph appears tidally disturbed (Ibata et al. 1995), and, soon after its discovery, it was realized that there was some tidal debris surrounding the galaxy (Mateo et al. 1996; Fahlman et al. 1996; Alard 1996; Ibata et al. 1997; Majewski et al. 1999). Indeed, it has been subsequently established that there are two huge tidal tails emanating from the edges of the galaxy and approximately tracing its orbital path, as expected from N-body simulations (Johnston et al. 1995; Ibata & Lewis 1998). These tails form a coherent and dynamically cold filamentary structure (hereafter Sgr Stream) that extends for tens of kpc from the parent galaxy and has been probed with many different tracers. Yanny et al. (2000) used SDSS first-year commissioning data to identify an overdensity of blue A-type stars in two stripes located at  $(l, b, D) = (341^\circ, +57^\circ, 46$  kpc) and  $(157^\circ, -58^\circ, 33$  kpc), which were subsequently found to match the prediction of the available theoretical models of the Sgr Stream (Ibata et al. 2001a). Similarly, Ivezić et al. (2000b) noticed that clumps of RR Lyrae stars in SDSS commissioning data lay along the Sgr orbit. The thorough study of the structure of the halo as traced by F stars from the SDSS, within a strip of  $\pm 1.26^\circ$  around the celestial equator, by Newberg et al. (2002) provided the first examples of Color Magnitude Diagrams (CMD) of the Stream population toward  $(l, b) = (350^\circ, 50^\circ)$  and  $(l, b) = (167^\circ, -54^\circ)$ . Other detections toward specific directions were provided by Martínez-Delgado et al. (2001, 2004), Bellazzini et al. (2003b) and Vivas & Zinn (2006). The first panoramic view of the Sgr Stream was presented by Ibata et al. (2002) using late M giants selected from the Second Incremental Data Release of 2MASS. Subsequently, Majewski et al. (2003, hereafter M03), having at disposal the final All Sky Data Release of 2MASS, used a larger sample of M giants to provide a clearer view of the whole complex, tracing very neatly the trailing tidal tail all over the Southern Galactic hemisphere, as well as the part of the leading arm closer to the main body of the galaxy, up to  $RA \simeq 190^\circ$ . In a very recent analysis Yanny et al. (2009a) showed that M and K giants can be successfully selected also from the SDSS and SEGUE datasets (Yanny et al. 2009b) and used to trace the Stream; one main advantage of using giants as tracers is that they can be (relatively) easily followed-up spectroscopically, thus providing crucial kinematical and chemical information

(Majewski et al. 2004; Monaco et al. 2007; Chou et al. 2007; Yanny et al. 2009a).

Bel06 exploited the SDSS data release 5 (DR5) to provide a picture of the leading arm of the Sgr Stream in the vicinity of the North Galactic Cap with remarkable clarity, using tracers (A-F dwarfs) that are intrinsically more numerous than M giants, for a given space density and/or surface brightness<sup>1</sup>. In their Fig. 1 they show the density of (candidate) A-F dwarf stars (selected with a simple color cut,  $g - r \leq 0.4$ , corresponding to  $\sim B - V \leq 0.6$ ) in the portion of the sky covered by the SDSS. The Sgr Stream emerges very clearly as a broad (and bifurcated) band going from  $(\alpha, \delta) \simeq (220^\circ, 0^\circ)$  to  $(\alpha, \delta) \simeq (125^\circ, 25^\circ)$ , where it plunges into the Galactic Disk. The color cut adopted by Bel06 is very successful in tracing the Stream structure as it takes advantage of the fact that Sgr stars are younger than typical halo stars, hence they have a bluer Turn Off (TO) color with respect to the halo population (see Unavane et al. 1996, for another application of the same principle). The density map by Bel06 shows evidence for a clear distance gradient along the Stream, from the nearest part crossing the Disk at  $\alpha \approx 120^\circ$ , to the most distant part at  $\alpha \approx 210^\circ$ , toward the North Galactic Pole (NGP). More recently, in a pilot project limited to a sub-sample of the SDSS (the so called Stripe 82) Cole et al. (2008) described a more refined approach to the study of the spatial structure of the Stream, using the same tracers as Newberg et al. (2002). Very recent detections from different data and/or using different models can be found also in de Jong et al. (2009), Prior et al. (2009b) and Keller (2009a).

In Bellazzini et al. (2006c, hereafter B06c) we demonstrated that yet another kind of tracer can be efficiently used to study the Sgr Stream, i.e. core-He-burning stars lying in the well populated Red Clump (RC) of the CMD of Sagittarius dSph. In particular, we showed that it is possible to detect the RC associated with a given sub-structure as a peak in the differential Star Count Profiles (SCP) of sub-samples of stars selected in a relatively narrow color range including the RC. The spatially localized RC population can be disentangled from the fore/background contaminating population of the MW by subtracting the underlying SCP, that is, in general, quite smooth and smoothly varying with position in the sky. In B06c we used this technique to compare the Horizontal Branch (HB) morphology in the Stream and in the main body of Sgr, finding an age/metallicity gradient along the Sgr remnant (see also Monaco et al. 2007; Chou et al. 2007), while in Correnti et al. (2009) we obtained an independent detection of the recently discovered stellar system Boötes III (Grillmair 2009; Carlin et al. 2009), providing new insight on its nature, structure and stellar populations. Carrell & Wilhelm (2010) recently presented the results of a spectroscopic survey targeting RC stars in the Sgr Stream, selected as in B06c.

<sup>1</sup> In a stellar population of given age and chemical composition the number of stars per units of sampled (integrated) luminosity in a given evolutionary phase is proportional to the duration of the evolutionary phase (see Renzini & Buzzoni 1986; Renzini & Fusi Pecci 1988; Renzini 1998, and references therein). A-F stars are evolving along the Main Sequence, a phase lasting several Gyr for these stars, while M giants are in the latest phases of their evolution along the Red Giant Branch, lasting  $\lesssim 10^8$  yr. Hence in any given field, independently of the absolute density normalization, A-F dwarfs outnumber M giants by a factor of  $\gtrsim 10$ .

The most natural and direct application of this technique is the determination of accurate distance estimates from the magnitude of detected RC peaks, as the RC is well known and widely used as a standard candle since long time (see Paczynski & Stanek 1998; Stanek & Garnavich 1998; Girardi & Salaris 2001; Babusiaux & Gilmore 2005; Bellazzini et al. 2006b, and references therein). For intermediate/old-age populations, the luminosity of the RC peak shows relatively modest variations as a function of age and metallicity, in particular when measured in the reddest optical passband (as Cousins'  $I$ , see Girardi & Salaris 2001). When used differentially, i.e. looking at the same (or very similar) stellar population in different places, the variations in the intrinsic luminosity of the RC due to age/metallicity effects should vanish. Given also the intrinsic narrowness of the feature in Sgr (see below), the RC seems the ideal tool to accurately trace the run of the distance along the orbital azimuth of the Sgr Stream, from the main body of the galaxy all over the portion of the Stream sampled by the SDSS. The other large survey covering all the extent of the Stream, 2MASS, cannot be used in this way as the associated photometry is not sufficiently deep to reach the RC level.

In this paper we will use the RC SCP method outlined above to take accurate *purely differential measures* of the distance of the Northern arms of the Sgr Stream with respect to the main body of the galaxy. This will provide strong constraints for the models of the disruption of Sgr within the Galactic (dark) halo, and, in turn on the physical properties of the dark halo itself (Ibata et al. 2001b; Helmi 2004; Johnston et al. 2005). The basic idea is the following: (a) we measure the position of the RC peak in  $V$  and  $I$ , with independent color selections using  $B - V$  and  $V - I$  colors, in the main body of Sgr (from B06a photometry), (b) we select SDSS fields projected onto the Sgr Stream as traced by Bel06, (c) we transform the SDSS photometry into  $B, V, I$  magnitudes, (d) we detect the RC peak(s) in  $V$  and  $I$  SCPs from the SDSS on-Stream fields (adopting the same color selections as in the main body), and (e) we obtain two independent measures of the magnitude differences of the RC peaks between the main body and the considered portion of the Stream. These are fully equivalent to differences in distance modulus, that is, differences in distance. The whole set of differential distances can be translated into a set of *absolute* distances by adopting the preferred value of the distance modulus for the main body (see, for example Alard 1996; Layden & Sarajedini 2000; Monaco et al. 2004; Kunder & Chaboyer 2009). The detection of the same peaks in both  $V$  and  $I$  SCPs provides a useful sanity check on the interpretation of the SCPs and on the derived differential distances. As an additional observational constraint to models of the disruption of Sgr, we provide also an estimate of the characteristic width of the Stream section crossed by our fields (see Sect. 3.5).

The plan of the paper is the following. In Sect. 2 we present the field of the main body that we used as template and the fields of the Stream used for/in the analysis. In Sect. 3 we describe the method used to analyze the SCPs and derive the informations from the peaks. In Sect. 4 we present all the SCPs obtained from each field and we discuss some special cases. In Sect. 5 we compare our results with previous works in literature, with par-

ticular emphasis on the different degree of uncertainty related to the distance estimates. In Sect. 6 we compare our distance estimates with models that reproduce the three-dimensional shape of the Stream. Finally, we summarize and discuss our results in Sect. 7.

Some preliminary reports on earlier phases of this project were presented in Correnti et al. (2007) and Correnti et al. (2008).

## 2. DATA AND OBSERVABLES

As a reference sample for the stellar population in the core of Sgr we take the photometry of a  $1^\circ \times 1^\circ$  wide field located  $\sim 2^\circ$  eastward of the galaxy center at  $(l, b) \simeq (6.5^\circ, -16.5^\circ)$ , presented in B06a and named *Sgr34*. This should be considered as fairly representative of the average population of the Sgr galaxy (see Bellazzini et al. 1999a,b; Giuffrida et al. 2010), avoiding the youngest and most metal-rich populations that appear to reside in the central nucleus (Siegel et al. 2007; Bellazzini et al. 2008). The strong similarity between the population of the Sgr main body and the Stream has been shown by Newberg et al. (2002) and Bel06, by direct comparison of CMDs<sup>2</sup>. To sample the Galactic population at similar angular distance from the Galactic Center as for *Sgr34* we used the same control field also presented in B06a: a  $0.5^\circ \times 0.5^\circ$  field, named *Gal\_Field*, at  $(l, b) \simeq (-6.0^\circ, -14.5^\circ)$ , that was used in B06a to perform the statistical decontamination of the *Sgr34* CMD from the foreground/background Galactic stars. Following B06a we adopted the average reddening values  $\langle E(B - V) \rangle = 0.116$  for *Sgr34* and  $\langle E(B - V) \rangle = 0.096$  for *Gal\_Field*, as derived from the reddening maps of Schlegel et al. (1998, hereafter SFD98).

To study the Stream, we used the SDSS-DR6 photometry of objects classified as stars (extracted from the SDSS CasJobs query system, Adelman-McCarthy et al. 2008)<sup>3</sup> for a series of selected fields along the branch A and B, listed in Tab. 1 and plotted in Fig. 1. We chose to follow the two branches separately, with non-overlapping fields. These on-Stream fields are similar, in position, to those studied by Bel06, but are slightly smaller ( $5^\circ \times 5^\circ$  instead of  $6^\circ \times 6^\circ$ ), to avoid overlap between different fields of the same branch. For each on-Stream field [located, for example, at  $(l, b) = (l_0, b_0)$ ] we selected also a corresponding *control field* (CF) located at the same latitude and at the same angular distance from the Galactic Center on the other side of the Galaxy [i.e. having  $(l, b) = (360^\circ - l_0, b_0)$ ]<sup>4</sup>. Assuming that the MW is symmetric about its center and its disk mid-plane (that should be a reasonable first-order approximation, at least at the Galactic latitudes considered here,  $b \geq 45.5^\circ$ ; but see Bell et al. 2008), each control field should be fairly representative of the typical Galactic population contaminating our on-Stream fields. Following Bel06, to average out the effects of shot noise, the control fields are larger than the on-Stream

<sup>2</sup> In particular, Bel06 uses the same photometry of *Sgr34* that is adopted here, as a reference.

<sup>3</sup> We used a template SQL query provided in the Cas-SDSS web page called “Clean Photometry”, in the version aimed at selecting stars. The corresponding SQL string can be found under the link *Clean Photometry* at <http://cas.sdss.org/astrodr7/en/help/docs/realquery.asp>.

<sup>4</sup> Except in the case of field F1B, for which the CF is the same adopted for the field F2B

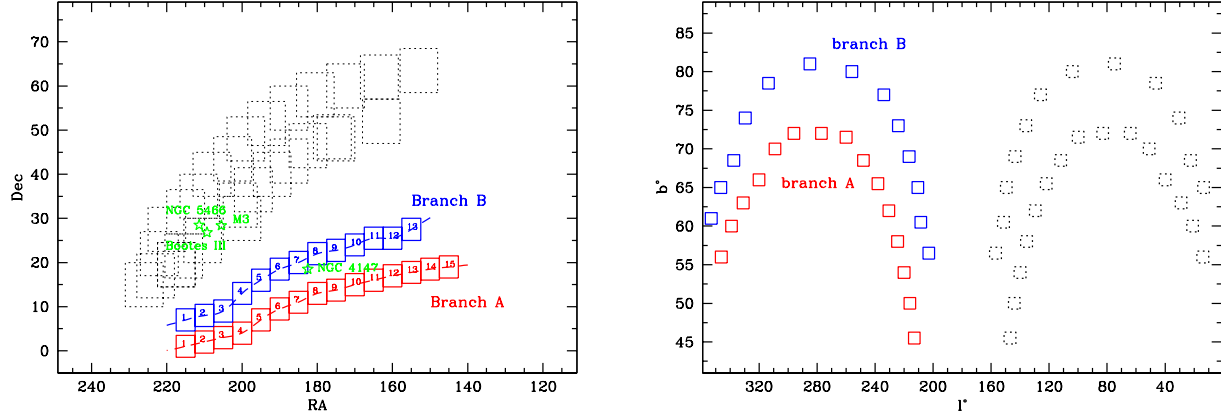


FIG. 1.— Left panel: Distribution of the on-Stream fields of the branch A (red squares) and the branch B (blue squares) of the Sgr Stream. The associated control fields are also plotted (black dashed squares). The plot is intended to show the position of the fields and give a rough idea of their dimension, projection effects are not taken into account. The shape of the two branches is reproduced with a continuous line, following Fig. 1 of Bel06. The positions of known stellar systems falling into the considered fields are indicated (green stars) and labeled. Right panel: Positions of the various fields in Galactic coordinates, to highlight the symmetry (with respect to the Galactic Center and to the Galactic Plane) of the adopted on-Stream fields and their corresponding Control Fields.

TABLE 1  
POSITION AND REDDENING OF THE CONSIDERED FIELDS<sup>a</sup>.

field	$\alpha$	$\delta$	$l^\circ$	$b^\circ$	$\langle E(B-V) \rangle$	$\sigma$	$\alpha_c$	$\delta_c$	$l_c^\circ$	$b_c^\circ$	$\langle E(B-V) \rangle_c$	$\sigma_c$
1A	215	1	346	56	0.038	0.007	226	15	14	56	0.034	0.009
2A	210	2	339	60	0.033	0.006	223	17	21	60	0.030	0.008
3A	205	3	331	63	0.026	0.003	222	22	29	63	0.034	0.008
4A	200	4	320	66	0.029	0.004	220	27.5	40	66	0.024	0.010
5A	195	7	309	70	0.031	0.005	215	31.5	51	70	0.015	0.004
6A	190	9.5	296	72	0.024	0.006	211.5	35	64	72	0.013	0.004
7A	185	11	277	72	0.027	0.007	208	40	83	72	0.010	0.004
8A	180	13	260	71.5	0.030	0.006	202.5	43.5	100	71.5	0.014	0.006
9A	175	13.75	248	68.5	0.037	0.007	199	48	112	68.5	0.014	0.005
10A	170	15	238	65.5	0.024	0.006	193.5	51.5	122	65.5	0.014	0.003
11A	165	16	230.5	62	0.022	0.005	187.5	55	129.5	62	0.015	0.004
12A	160	17	224.5	58	0.030	0.006	180.5	58	135.5	58	0.017	0.007
13A	155	17.75	220	54	0.031	0.007	172.5	60	140	54	0.014	0.007
14A	150	18.5	216	50	0.030	0.004	163.5	62	144	50	0.011	0.006
15A	145	19	213	45.5	0.030	0.006	153	63.5	147	45.5	0.017	0.016
1B	215	7	353	61	0.027	0.003	217.5	19.5	13.5	65	0.029	0.008
2B	210	8	346.5	65	0.026	0.003	217.5	19.5	13.5	65	0.029	0.008
3B	205	9	337.5	68.5	0.028	0.004	215.5	21.5	22.5	68.5	0.028	0.008
4B	200	13	329.5	74	0.025	0.004	210.5	25	30.5	74	0.019	0.007
5B	195	16	313.5	78.5	0.027	0.006	200	30	46.5	78.5	0.012	0.002
6B	190	18.5	285	81	0.025	0.005	201	33	75	81	0.012	0.002
7B	185	20	256	80	0.029	0.005	197	36.5	104	80	0.013	0.003
8B	180	22	234	77	0.028	0.006	192	40	126	77	0.016	0.004
9B	175	22.75	224	73	0.023	0.004	187.5	43	136	73	0.017	0.005
10B	170	24	216.5	69	0.017	0.002	182.5	46.5	143.5	69	0.017	0.005
11B	165	25.5	210.5	65	0.022	0.008	176	48.5	149.5	65	0.019	0.005
12B	160	25.5	208.5	60.5	0.025	0.007	175	48	151.5	65	0.018	0.005
13B	155	27.5	203	56.5	0.028	0.007	163	52	157	56.5	0.013	0.004

<sup>a</sup> $\langle E(B-V) \rangle$  is the mean reddening of the field as extracted from Schlegel et al. (1998) maps and averaged over all the stars in the field;  $\sigma$  is the corresponding standard deviation. The subscript  $c$  refers to *control fields*.

fields ( $10^\circ \times 10^\circ$ ). As shown in Fig. 1, the globular clusters NGC5466 and M3, and the dwarf galaxy remnant Boötes III are enclosed within some of our control fields (Correnti et al. 2009). To avoid any undesired contamination we excluded from the corresponding samples the stars associated with these stellar systems by excising areas of radius  $1^\circ$  (for the globulars) and  $2^\circ$  (for the dwarf galaxy) around their centers. The only known stellar system that is (partially) enclosed in one of our on-Stream fields is the globular cluster NGC4147 (see Bel06 and Bellazzini et al. 2003a,b). Also in this case we excluded from the adopted sample all the stars within  $1^\circ$  of the cluster center. In the following we will use CFs only as a further observational check that the simple models we

adopt to account for the fore/background populations contaminating our SCPs are adequate for our purposes (see Sect. 3.1).

For our analysis we adopted the reddening-corrected  $g, r, i, z$  magnitudes as provided by CasJobs. These magnitudes were also corrected using the SFD98 maps, hence the source of the reddening corrections is homogeneous for all the datasets considered in the present analysis. The mean  $E(B-V)$  and its standard deviation for each field, averaged over all the stars included in the field, are reported in Table 1. It is important to note that the average reddening of our fields is remarkably low ( $0.010 \leq E(B-V) \leq 0.038$ ) and constant within each field ( $0.002 \leq \sigma_{E(B-V)} \leq 0.010$ ), hence any error in

the adopted reddening correction would have only a minor impact on our final *differential distance* estimates. For brevity, in the following all the reported magnitudes and colors are reddening-corrected (i.e., for example,  $V = V_0$  = extinction corrected  $V$  magnitude).

The  $g, r, i, z$  magnitudes in the SDSS system have been transformed to the Johnson-Kron-Cousins  $B, V, I$  system (as defined by the standard stars by Landolt 1992) using robust empirical transformations that have been checked to be particularly accurate in the color range typical of RC stars (provided by Lupton 2005<sup>5</sup>, derived from large samples of stars in common between SDSS and the extended database of Landolt's standards by Stetson 2000). In particular, we obtain  $B$  and  $V$  from  $g$  and  $r$ , while  $I$  is obtained from  $i$  and  $z$ , adopting the following equations:

$$B = g + 0.3130(g - r) + 0.2271 \quad \sigma = 0.0107 \quad (1)$$

$$V = g - 0.5784(g - r) - 0.0038 \quad \sigma = 0.0054 \quad (2)$$

$$I = i - 0.3780(i - z) - 0.3974 \quad \sigma = 0.0063 \quad (3)$$

Note that the transformed  $V$  and  $I$  are *fully independent* as they are obtained by independent couples of SDSS magnitudes. Consequently, measures of the position of any significant peak detected in  $V$  and  $I$  SCPs will also be independent, thus providing a powerful cross-check of any detection and distance estimate.

### 2.1. Selections on the Color Magnitude Diagram

In Fig. 2 we present reddening-corrected  $V, B-V$  and  $I, V-I$  CMDs (focused on the RC features up to the upper region of the Main Sequence, MS) of the main-body field *Sgr34* and of the corresponding control field *Gal\_Field*. The comparison between the CMDs of the two fields permits the identification of the main features associated with Sgr and with the fore/background Galactic populations. The RC of the Sagittarius dSph is a prominent feature in the CMDs of the *Sgr34* field (upper panels), around  $(I, V - I) \simeq (16.9, 0.9)$  and  $(V, B - V) \simeq (17.8, 0.8)$ . The wide and inclined Red Giant Branch (RGB) can be discerned over the background, going from  $(I, V - I) \simeq (16.9, 0.9)$  to  $(I, V - I) \simeq (14.0, 1.5)$  [ $(V, B - V) \simeq (19.5, 0.8)$  to  $(V, B - V) \simeq (16.0, 1.4)$ ], and continuing beyond the limits of the box. The RGB bump is apparent at  $V \sim 18.2$  and  $I \sim 17.2$ , along the RGB (see Monaco et al. 2002). For  $V - I \lesssim 0.3$  ( $B - V \lesssim 0.2$ ) at  $I \sim 19.0$  ( $V \sim 17.9$ ) a portion of the Blue Horizontal Branch (BHB) is also visible (Monaco et al. 2003); at  $V - I \lesssim 0.5$  ( $B - V \lesssim 0.4$ ) and  $I \gtrsim 19.5$  ( $V \gtrsim 18.5$ ) the Blue Plume (BP, Mateo et al. 1995b; Bellazzini et al. 1999a, B06a) population is visible. The Sub Giant Branch (SGB, for  $V - I \gtrsim 0.8$  or  $B - V \gtrsim 0.7$ ) and the upper Main Sequence (MS, to the blue of the above limits) appear for  $I \gtrsim 19.0$  ( $V \gtrsim 20.0$ ). For a more detailed description of the CMD of Sgr see B06a. The strong vertical band around  $V - I \sim 0.7$  ( $B - V \sim 0.6$ ) running over the largest part of the CMD, and bending to the red at  $I \sim 19$ ,  $V \sim 20$ , is constituted by MS stars of the MW (mostly from the Thick Disk, in this direction, according to the Galactic model by Robin et al. 2003); the wide band running parallel, to the red of the vertical portion of this feature is mainly populated by Galactic

giants, either in their RGB or RC/HB phase. The majority of the stars redder than  $V - I = B - V \sim 1.0$  belongs to the vertical plume of local Galactic M dwarfs.

The vertical lines in each panel of Fig. 2 enclose the color stripes that we adopted to select the RC population in the two colors, corresponding to  $0.70 \leq B - V \leq 0.95$  and  $0.85 \leq V - I \leq 1.05$ . The choice of the color limits was made in order to include the bulk of the RC population even if small color shifts were present due to errors in the adopted reddening corrections and/or population gradients, while keeping the contamination from other sources as low as possible. The distribution in color within the selection windows (around the magnitude of the observed RC of Sgr) shown in Fig. 3 suggests that color shifts of order  $\pm 0.05$  mag would lead just to minor losses of the signal (of the order of 10% with respect to the number of stars obtained with our choice in the selection window).

Fig. 2 clearly shows that, in addition to Sgr RC stars, several different contaminants are expected to enter the selection window. For  $I \leq 18.5$  ( $V \leq 19.5$ ) Galactic giants (mainly RC stars) should be the primary source of contamination, while the sequence of Galactic MS stars crosses the selection stripes at  $I \gtrsim 19$  and  $V \gtrsim 20$ , boosting the star counts at faint magnitudes. The RGB of the Sgr population, and in particular the RGB bump, are also selected by the adopted windows. We will show below that this source of contamination has a negligible effect on our SCPs. At  $I \gtrsim 19.0$  ( $V \gtrsim 20.0$ ) the SGB stars of Sgr enter the selection window; as they are much more numerous than RGB and RC stars they may provide a serious contribution to the “background” in our SCPs, at faint magnitudes. Finally, the MS of Sgr crosses the windows at  $I \gtrsim 21$  ( $V \gtrsim 22$ ). The actual structure of the contamination entering the windows will obviously depend on (a) the Galactic population encountered along the considered line of sight (*los*, hereafter), and (b) the distance of the wrap(s) of the Sgr Stream that is(are) crossed by the considered *los*. However the *los* considered in this study are all at much higher Galactic latitudes than *Sgr34*, hence the degree of contamination per unit area of the sky should be lower, and the average distance of the encountered stars should be higher, hence most of the contamination by Galactic dwarfs should occur at fainter magnitudes than discussed above for *Sgr34*. Furthermore, all the detections of the Stream presented here are at distances similar or larger than the main body of the galaxy sampled by *Sgr34*; hence, in most cases the contamination by the SGB of the Stream population will occur at fainter magnitudes than in *Sgr34*<sup>6</sup>. In any case, to limit the contribution by dwarf stars, independently of their origin, we limit our analysis to the magnitude ranges  $15.0 \leq I \leq 19.5$  and  $16.0 \leq V \leq 20.5$ <sup>7</sup>. These limits approximately correspond to an accessible range of heliocentric distances  $12 \text{ kpc} \lesssim D \lesssim 70 \text{ kpc}$  (see Fig. 5, below).

<sup>6</sup> However it should be noted that the MS of wraps of the Streams that are too nearby to have their RC detected with the present technique may contribute to the contamination of our color-selected samples of candidate RC stars. Moreover, other unknown substructures may contribute to the contamination (see Correnti et al. 2009, for example).

<sup>7</sup> Except in the case of *Sgr34* where the limits are  $15.0 \leq I \leq 18.5$  and  $16.0 \leq V \leq 19.5$

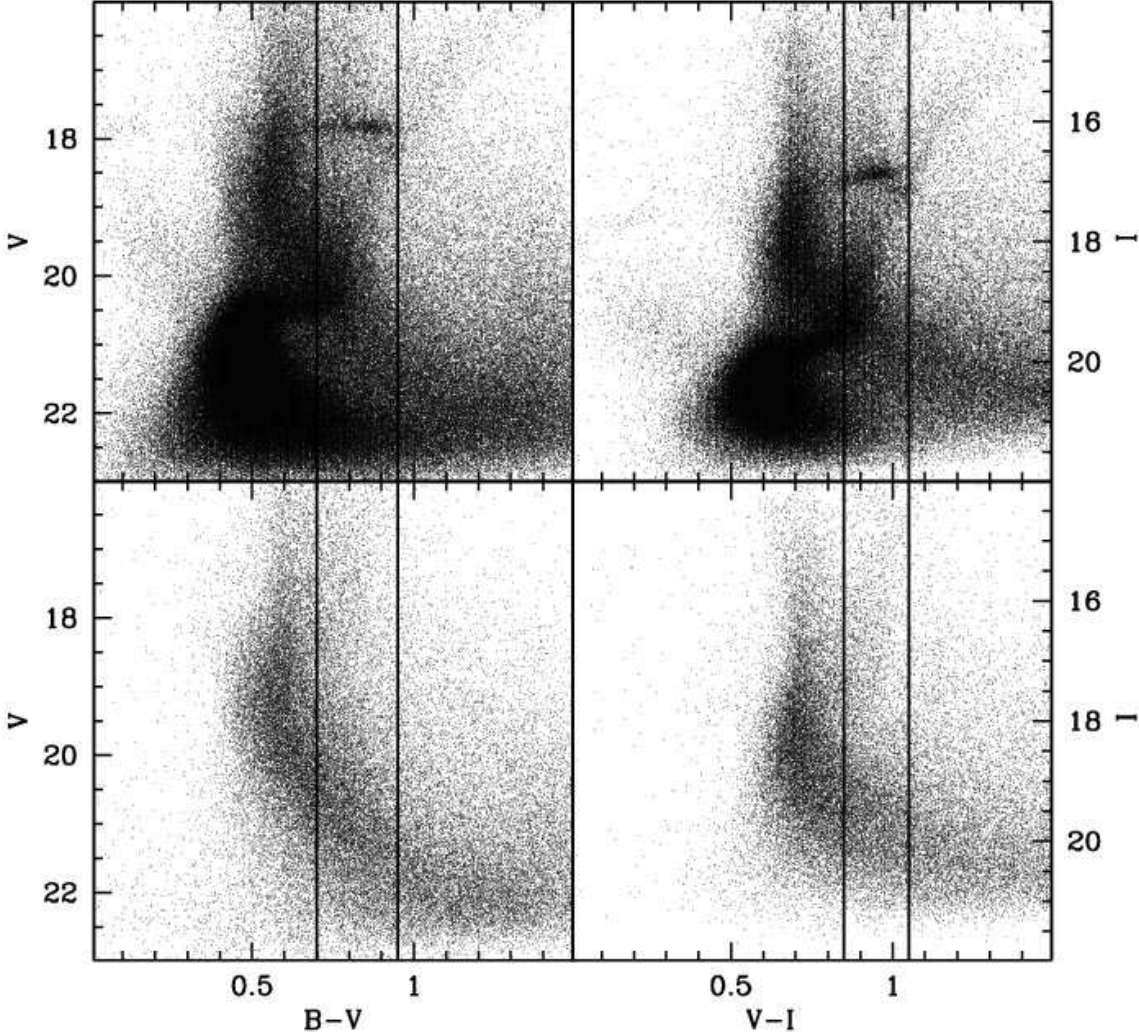


FIG. 2.— Reddening corrected ( $V, B-V$ ; left panels) and ( $I, V-I$ ; right panels) CMDs, focused on the RC up to the upper part of the MS, of the Sgr field (*Sgr34*, upper panels) and of the control field (*GalField*, lower panels). The vertical lines enclose the RC populations and are the color strips used to select the region where build the SCPs. The color ranges are respectively,  $0.70 \leq (B - V) \leq 0.95$  and  $0.85 \leq (V - I) \leq 1.05$ .

While the surface brightness of Sgr at *Sgr34* is  $\sim 25$  mag/arcsec $^2$ , typical values for the Stream are  $\gtrsim 30$  mag/arcsec $^2$  (Mateo et al. 1998; Bellazzini et al. 2003b; Majewski et al. 2003, and references therein). It may be quite hard to identify the feeble signal from such sparse populations even in the presence of low background. In fact, even in the most favorable cases, the RC is barely visible in the CMDs of on-Stream Fields (see, e.g. Newberg et al. 2002). The construction and modeling of SCPs described below is very effective in extracting the distance information in these cases (B06c, Correnti et al. 2009).

Finally, there are several indications that there is a sizable metallicity (and presumably age) gradient along the Stream, in the sense that the average metallicity is lower in distant portion of the Stream with respect to the main body of Sgr (B06c, Monaco et al. 2007; Chou et al. 2007). This is generally interpreted as due to a pre-existing population gradient within the original body of the Sgr galaxy, as the tidal tails were preferentially populated by stars that resided in the old and metal poor outskirts of Sgr (Chou et al. 2007). It must be stressed that the detected gradient means that the relative pro-

portion of *intermediate-age & metal-rich stars* and of *old-age metal-poor stars* changes along the Stream (and with respect to the main body). This, in turn, changes the HB morphology, i.e. the relative abundance of RC and Blue HB stars (as observed in B06c), but is it not expected to change the intrinsic luminosity of the RC. Indeed, Carrera & Wilhelm (2010) find that the mean metallicity of RC stars along the Stream is very similar to that found in the main body of Sgr. Hence, while the population gradient may bias estimates of the stellar density along the Stream obtained from RC stars, our distance estimates should be unaffected and our characteristic size estimates can be only marginally affected (see Sect. 3.5 and Fig. 18, below, for further details and discussion).

## 2.2. Detecting RC peaks in Star Count Profiles

All the SCPs of color-selected RC samples presented in this paper are computed as running histograms (see Bellazzini et al. 2005, and references therein)<sup>8</sup>, as these couple the property of collecting the signal from a wide

<sup>8</sup> Running histograms are histograms in which the step is smaller than the bin width. The adoption of steps much smaller than the bin width removes the dependency from the starting position of

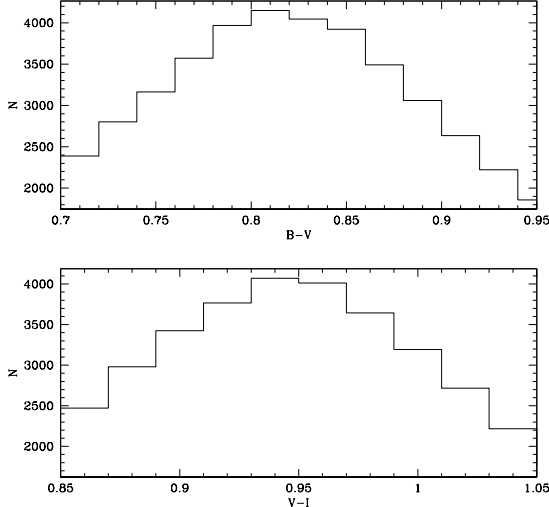


FIG. 3.— Distribution of stars in  $B-V$  (upper panel) and  $V-I$  (lower panel) color stripes for the  $Sgr34$  field. The selection must be optimized in order to contain all the RC stars, but minimizing the presence of contaminating stars. The RC is well confined inside the selected regions and peaks near the middle in both; the magnitude limits of the selection are respectively,  $17.3 \leq V \leq 18.3$  and  $16.4 \leq I \leq 17.4$ .

bin with the ability of constraining with great accuracy the location of density maxima, almost independently of the bin width. A bin width of  $\pm 0.2$  mag<sup>9</sup> and step of 0.02 mag have been adopted here. After different trials, they have been found to provide a good compromise between the exigence of co-adding all the signal from a given RC population (that requires larger bins) and the ability of distinguishing (resolving) nearby peaks (that is favored by smaller bins). The use of generalized histograms (Laird et al. 1988) would have provided an higher degree of smoothing, possibly making some of our SCPs easier to interpret. However we preferred running histograms as they provide the reader a clearer idea of the local noise on the SCP as well as a scale in real units ( $\frac{\text{stars}}{\text{mag bin} \times \text{FoV}}$ ). The density scales of the various fields have all been reported to unit standard area ( $1^\circ \times 1^\circ$ ) by applying the corrections due to spherical geometry that is inherent to equatorial coordinates.

To illustrate at best the case of the detection of the RC of a spatially confined stellar system in a color-selected SCP, we show in Fig. 4 the  $V$  and  $I$  SCPs for the  $Sgr34$  field (continuous lines), compared with those obtained for the control field  $Gal\_Field$ , normalized by the ratio of background densities between the two fields<sup>10</sup>.

The shapes of the  $Sgr34$  and  $Gal\_Field$  SCPs are *remarkably similar*: the only exception is the very strong and well defined peak corresponding to the RC of the Sgr galaxy seen in Fig. 2. It is interesting to note that

the binning that affects classic histograms. Clearly, the values of adjacent bins are not statistically independent.

<sup>9</sup> With rare exceptions in which bins of  $\pm 0.25$  mag have been adopted to enhance the signal of a weak feature. All these cases are clearly indicated in the following.

<sup>10</sup> This ratio is dominated by the ratio of the areas of the fields,  $Sgr34$  being  $\simeq 4$  times larger than  $Gal\_Field$ . However  $Gal\_Field$  sample a direction  $\simeq 2^\circ$  closer to the Galactic Plane and  $\simeq 0.5^\circ$  closer to the Galactic Center than  $Sgr34$ , hence the (column) stellar density is intrinsically larger in the former field. The actual density ratio, computed in selected CMD boxes where the contribution from Sgr dSph stars is negligible, is  $\simeq 3$ , see Bellazzini et al. (1999b) and B06a.

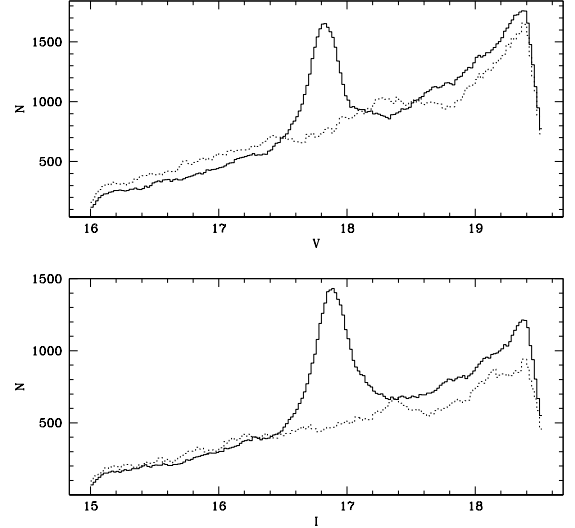


FIG. 4.— De-reddened running histogram SCPs of color-selected RC candidates for  $Sgr34$  (continuous line) and for the control field  $Gal\_Field$  (dashed line) in  $V$  and  $I$  magnitude (respectively upper and bottom panel). The shape of the SCPs is similar but, as expected, in the  $Gal\_Field$  the peak is completely lacking, while in the Sgr field it stands out very clearly.

while also other features related to Sgr are visible in the CMDs and (at least partially) included in the selection windows, as for example the RGB bump, in the SCPs the RC is the only signal emerging from the Sgr population. Independently of the origin of the stellar mix actually selected, the SCP of the control field, and, by analogy, the SCP of the contaminating population that is superposed on the RC in the  $Sgr34$  SCP, are quite smooth and have a very simple behavior; in B06c, Correnti et al. (2009) and in Sect. 3.1 we show that this is the general behavior of the SCP of the back/foreground population in the vast majority of the considered *los*, thus justifying the choice of a very simple model for them, as described in Sect. 3, below.

### 2.3. Sensitivity of the technique

Before proceeding with the description of the method adopted to obtain the actual differential distance estimates, it may be useful to study the sensitivity of our SCPs to the various properties of any encountered substructure (distance, density, etc.). To do that we used the dedicated web tool<sup>11</sup> of the BASTI repository of stellar models (Pietrinferni et al. 2004; Cordier et al. 2007) to produce a synthetic population of  $\sim 45000$  stars having age and metallicity similar to the bulk of the Sgr population (age=6 Gyr,  $[Fe/H] = -0.5$ ). The CMD and the color-selected RC SCP of the population are shown in the left panels of Fig. 5. The synthetic stars have been distributed along the line of sight according to gaussian distributions having various mean distances ( $D=15, 25, 40$  and  $65$  kpc) and Full Width at Half Maximum (FWHM) of 3.3 kpc or 6.6 kpc, to simulate the crossing of a wrap of the Stream at various distances and with different characteristic sizes along the *los*. A  $FWHM \simeq 3.3$  kpc is quite typical of sections of Stream wraps crossed perpendicularly by a given *los*, as measured on the models of the disruption of the Sgr galaxy by Law et al. (2005). The  $FWHM \simeq 6.6$  kpc has been considered to account

<sup>11</sup> <http://albione.oa-teramo.inaf.it>

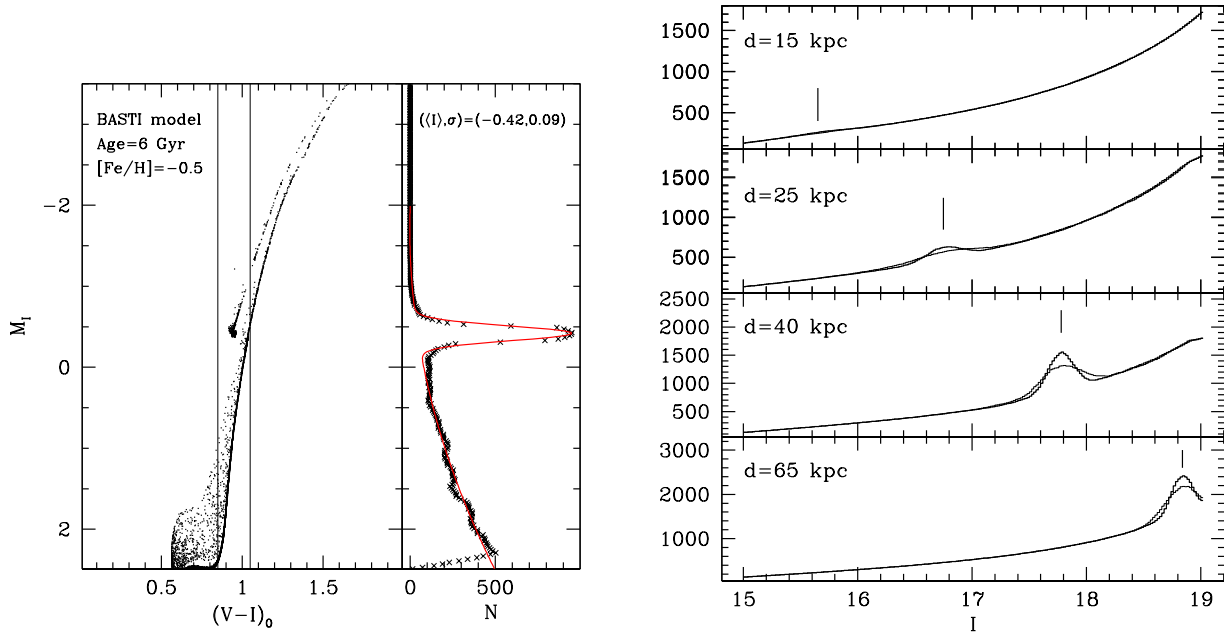


FIG. 5.— (a). Left panel: CMD of a synthetic population composed of 45953 stars having age=6 Gyr,  $[Fe/H] = -0.5$ , solar scaled abundance pattern, 10% of binary systems, and Salpeter's Initial Mass Function, from the BASTI database. The color window adopted to select RC candidates is enclosed within the two thin parallel lines. Right panel: SCP of the color-selected RC candidates obtained in the same way as Fig. 4 (x symbols) and fitted with the same kind of model (red continuous line). The mean and standard deviation of the best-fitting Gaussian are reported within parentheses. (b). The synthetic population shown in panel(a) has been distributed along the line of sight according to gaussian distributions having various mean distances ( $D=15, 25, 40$  and  $65$  kpc, from the upper to the lower panel, respectively) and Full Width at Half Maximum of  $3.3$  kpc (thick lines) or  $6.6$  kpc (thin lines). The SCP of the resulting color-selected RC population has been derived and superposed to the (model) SCP of the background of Fig. 4, to simulate the detection of the same structure at different distances with the method applied here. The vertical segments indicate the positions of the peaks produced by the considered structures.

for cases of sparser portions of the Stream and/or non-perpendicular intersections with the *los*. The SCPs of the resulting color-selected RC population have been derived (properly including realistic photometric errors<sup>12</sup>) and added to the SCP of the background of Fig. 4, as modeled in Fig. 6, below, to simulate the detection of the same structure with the method applied here. The results of this simulation are shown in the right panels of Fig. 5.

The most obvious effect shown in Fig. 5 is the increase of sensitivity with the distance of the structure. This is due to two factors: (1) the inherent “compressive” property of the magnitude scale, by which, for instance, a difference in distance of  $3.3$  kpc corresponds to a difference in magnitudes of  $0.43$  mag at  $D=15$  kpc and to just  $0.14$  mag at  $D=50$  kpc, and (2) the relative dimension of the considered structure and of the *los* cone at the distance of the structure; for nearby structures the fixed FoV adopted here may be smaller than the structure itself, thus missing part of the signal that instead would be included when more distant structures are encountered. This effect illustrates a fundamental property of our method that should always be taken into account: a structure that is very cleanly detected at, say,  $D=30$  kpc may go completely undetected if located at  $D=15$  kpc, instead. This implies that while significant detections of RC peaks in our SCPs are robust and provide accu-

rate distances, the significance of non-detections must be evaluated with great care, on a case by case basis, and, in general cannot be taken as a proof of the *absence* of a given structure (that, for example, may be predicted by some model). One can conceive various different techniques to mitigate this dependence of sensitivity on distance, as, for example, to scale the bin width with magnitude to account for the effect described at point (1), above, or to transform the magnitudes of any color-selected RC candidate into distances, by assuming template values for  $M_I$  and  $M_V$ , and then to search for peaks in Distance Functions instead of SCPs. However each of these possible solutions would have an impact on the accuracy of the derived distance scale: for this reason we prefer to maintain an approach that derives differential distances from the direct comparison of truly *observable* quantities of strictly the same nature, i.e. the magnitudes of peaks in SCPs that can be determined to within a few hundredths of mag, finally providing differential distances with accuracies  $< 10\%$ . Other methods to trace structures are intrinsically more powerful for other purposes (like the *detection* of structures, for example; see Bel06). The technique adopted here is best suited for distance measures and we decided to optimize it to this task, at least in the present application.

### 3. MODELING OBSERVED SCPs AND MEASURING DIFFERENTIAL DISTANCES

In the following we will describe the technique that we use to accurately estimate the magnitude (and the statistical significance) of peaks in the SCP of on-Stream fields. To illustrate it we recur again to the case of the *Sgr34* field (we will show below also two cases of on-

<sup>12</sup> For each passband, we fitted the error curve derived from SDSS photometric errors with exponential functions. Then we used the fitted functions to assign the proper average error to each synthetic star (according to its magnitude) and we added to each synthetic magnitude an error component extracted from a gaussian distribution having  $\sigma$  equal to the average error.

Stream fields). The approach is strictly the same for  $V$  and  $I$  SCPs and it is presented in parallel in the left and right columns of panels of Fig. 6:

1. Upper panels: a possible RC peak is detected in both SCPs. The underlying smooth SCP (the back/foreground component) is fitted with a simple function of the form  $f(x) = Ae^x + Bx + C$ , once the points in the range enclosing the peak are excluded (see also B06a and Correnti et al. 2009). This simple procedure is very effective in all the cases considered here and it allows a reliable interpolation of the background in the region of the peak. The dotted lines mark the  $3,4$  and  $5\sigma$  levels above the background, that are computed including both the Poisson noise and the uncertainty in the fit of the background component (that is conservatively assumed to be of the same order of the Poisson noise, i.e.  $\sqrt{N}$ , where  $N$  is the value of the model at a given position). To verify the validity of our assumption for running histograms (that have non-independent bins), we made several trials (in different fields) using “classical” histograms, where Poisson statistics clearly apply. We found that the statistical significance lines are at the same level in both classical and running histograms, confirming that our simple assumptions lead to correct results (see as another example of the same approach Correnti et al. 2009).
2. Middle panels: the model of the background ( $f(x)$ ) is subtracted from the observed SCP. The only significant residual is the RC peak that, in general, has a rather symmetric bell shape. The peak is fitted with a gaussian curve ( $G(x)$ ) by searching for the three parameters of  $G(x)$  (mean,  $\sigma$  and normalization factor) that minimize the reduced  $\chi^2$ . The derived mean is taken as the best estimate for the position of the considered peak. As the bins of the adopted running histogram are not independent, the resulting  $\chi^2$  values can be considered only in a relative sense. After several trials on real cases we found that increases of  $\chi^2$  by a factor of 2 with respect to the best solution (having  $\chi^2 = \chi^2_{min}$ ) always correspond to clearly unsatisfactory fits (see Fig. 9, for an example). For this reason we adopt the difference between the best-fit mean and the mean of the solutions having  $\chi^2 = 2\chi^2_{min}$  as a robust estimate of the accuracy of our measures. As a sanity check we tested the assumed models against the corresponding ordinary histogram (i.e. with independent bins) for nine flag=1 peaks, computing the actual  $1\sigma$  uncertainty. It turned out that our empirically defined error is always within a factor from 0.5 to 2 times the statistically correct  $1\sigma$  error, thus providing a realistic estimate of the uncertainty of our measures.
3. Lower panels: the global model, obtained by summing  $f(x)$  and  $G(x)$ , is compared to the observed SCPs. This final form of the overall fit is what we will show for all the considered fields in Sect. 4, below. In Sect. 3.1 we will show that the adopted model of the fore/background component of the

considered SCPs ( $f(x)$ ) provides an adequate representation of what is observed in actual CFs and predicted by current Galactic models.

The application to the *Sgr34* field just described, provides also the Zero Points of our differential distance scale, i.e. the magnitude of the RC in the main body of Sgr,  $V = 17.82 \pm 0.02$  and  $I = 16.87 \pm 0.02$ . As a sanity check, we verify if these numbers are compatible with theoretical stellar model predictions<sup>13</sup>. Adopting the distance modulus  $(m - M)_0 = 17.10 \pm 0.15$  for Sgr (Monaco et al. 2004) we obtain  $M_I = -0.23 \pm 0.15$  and  $M_V = +0.72 \pm 0.15$ . These correspond to ages in the range 5-7 Gyr for  $[Fe/H] = -0.4$  and 9-11 Gyr for  $[Fe/H] = -0.7$  in the models by Girardi & Salaris (2001), in good agreement with all recent estimates of the typical age of the bulk of the Sgr stars (see Layden & Sarajedini 2000; Monaco et al. 2002, B06a).

### 3.1. The SCPs of Control Fields

To verify empirically that the peaks we interpret as due to intersections of the considered *los* with Stream wraps are not due to Galactic structures, we have inspected all the color-selected SCPs of the Control Fields described in Sect. 2. The overall conclusion is that there is nothing similar to the peaks we observe in the SCP of our on-Stream fields in generic Galactic fields at similar distances from the plane and the center of the Galaxy.

In Fig. 10 we show various examples: the SCPs of six on-Stream fields (continuous lines) are compared to the SCPs of their corresponding CFs (dotted lines, see Fig. 1). The best-fit models for the on-Stream SCPs, together with the background and the  $3\sigma$  levels are also reported, using the same symbols as in Sect. 3 and Sect. 4 below. The two SCPs are normalized by the ratio of the sampled areas, but any other reasonable normalization (for example, by the ratio between the number of stars that fall inside our color selection) does not significantly change the results.

The shapes of the SCPs are very similar in the range not affected by the peaks associated with the Stream, as already observed when we have done the same comparison in the main body (Fig. 6). It is quite clear that the strong and well defined peaks observed in on-Stream fields are lacking in the SCPs of Control Fields (however there is no guarantee that genuine and yet unrecognized structures are present also along these *los*). It is also reassuring to note that the models for the SCP of the contaminating back/foreground population we have adopted for the on-Stream fields provide a good description also of the CF SCPs, at least out to  $V \simeq 18.5$ . Beyond this limit it is quite clear that in the on-Stream fields there is an additional source of contamination, that has to be ascribed to RGB, SGB and MS stars from the Stream population itself, as discussed in Sect. 2.1. This provides further support to the idea that the adopted approach of fitting the back/foreground component directly on on-Stream SCPs is the most effective way to get rid of this

<sup>13</sup> That, however, are quite uncertain and model dependent, in an absolute sense, for stars in this evolutionary phase. For instance the absolute  $I$  magnitude of the peak for a age=6 Gyr,  $[Fe/H] = -0.5$  model from the BASTI dataset (shown in Fig. 5), is matched by a model of age=1.7 Gyr and  $[Fe/H] = -0.4$ , from the set by Girardi & Salaris (2001).

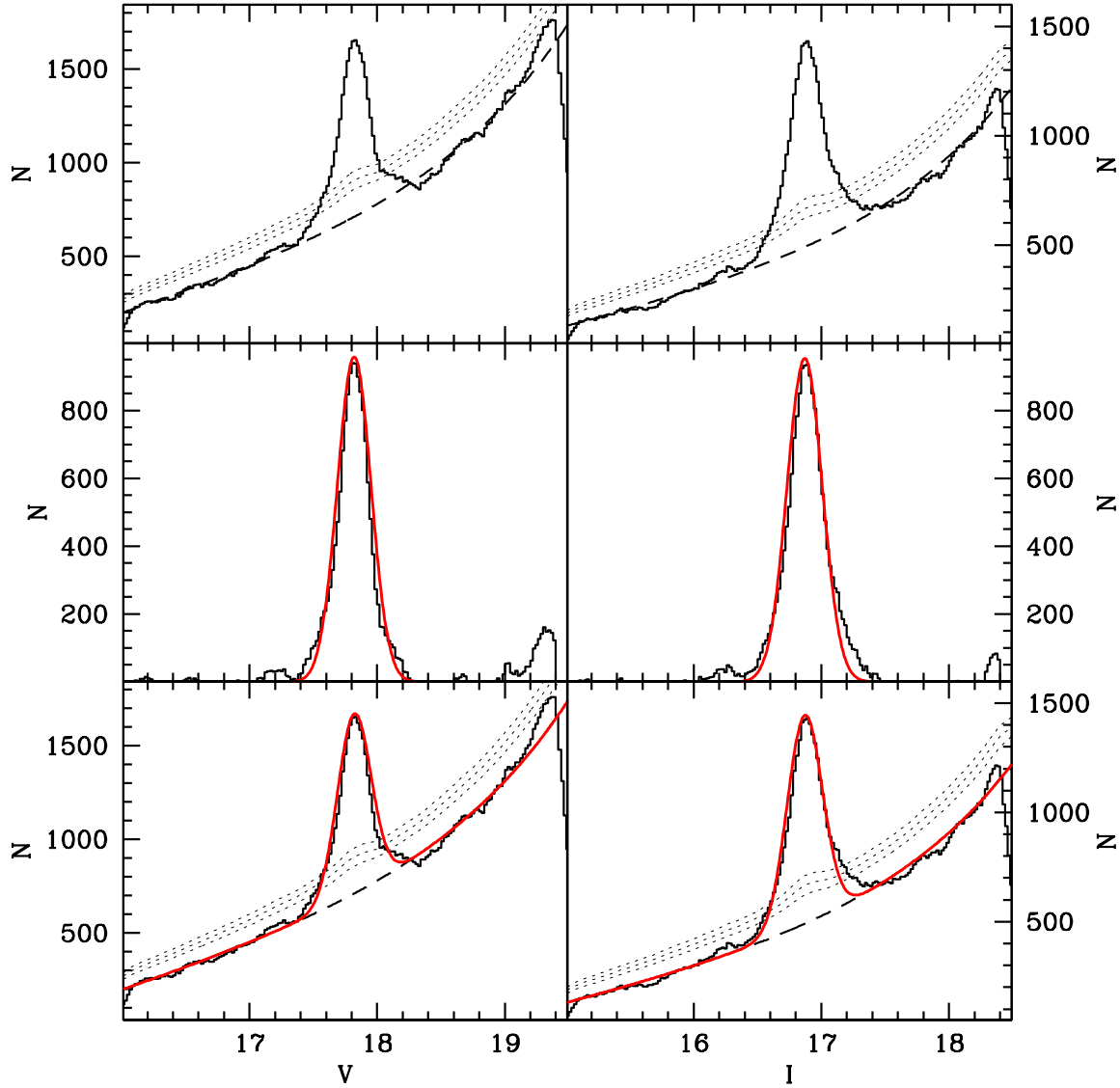


FIG. 6.— Upper panels: de-reddened running histogram SCPs of color-selected RC candidates for the *Sgr34* field (continuous line) in *V* and *I* magnitude (left and right panel, respectively); the dashed line represents the polynomial fit of the background ( $f(x)$ ). The dotted lines mark the 3.4 and 5 $\sigma$  levels above the background, that is computed including both the Poisson noise and the uncertainty in the fit. Middle panels: Residuals of the subtraction between the observed SCPs and the fit of the SCPs without the peaks; in red we plotted the fit of the peaks, obtained with a gaussian ( $G(x)$ ). Bottom panels: same as the first ones, with added in red the total fit of the SCPs (polynomial for the bkg + gaussian for the peaks,  $f(x) + G(x)$ ).

kind of self-containment from other species of Stream stars, that would not have been possible if we merely subtracted the CF SCPs to the on-Stream ones.

In the lower right panel we present the case of F15A, that will be discussed in Sect. 4.1. It is interesting to note the close similarity between the two considered SCPs for this field, where we do not detect any signal from the Stream, and they are therefore expected to be (both) dominated by the generic halo/thick disk Galactic population.

### 3.2. Examples of on-Stream fits

In Fig. 7 and Fig. 8 we show two examples of application to on-Stream fields, the fields F7A and F5A, respectively. In the first case a broad peak with significance above 4 $\sigma$  is detected in both the *V* and *I* SCPs. The derived differential distances with respect to the main body are in good agreement, within the uncertainties.

The  $f(x) + G(x)$  model provides an excellent description of the observed SCPs.

Two significant peaks are detected in the SCPs of the field F5A (Fig. 8), thus, in this case, we need a model with two gaussian components. Both peaks are significantly narrower than that found in field F7A. Nevertheless the model  $f(x) + G_1(x) + G_2(x)$  provides an excellent representation of the observed SCPs. The differential distances obtained from the *V* and *I* SCPs are in good agreement: there is no doubt that we are detecting *the same structures in both SCPs*.

To place the results shown in Fig. 7 and Fig. 8 into the proper context, we plot the positions of the detected peaks into the  $X_{\odot, \text{Sgr}} Y_{\odot, \text{Sgr}}$  plane of the heliocentric Sgr coordinates as defined by Majewski et al. (2003), in Fig. 11. This plane is defined to coincide with the plane of the orbit of Sgr, hence the Stream is expected to be confined within a few kpc about it. We compare

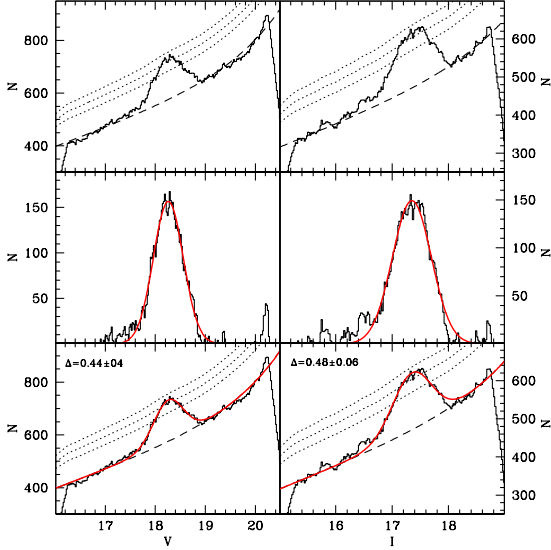


FIG. 7.— Upper panels: de-reddened running histogram SCPs of color-selected RC candidates for a Stream field (field F7A, continuous line) in  $V$  and  $I$  magnitude (left and right panel, respectively); the dashed line represents the polynomial fit of the background ( $f(x)$ ). The dotted lines mark the 3,4 and  $5\sigma$  levels above the background, that is computed including both the Poisson noise and the uncertainty in the fit. Middle panels: Residuals of the subtraction between the observed SCPs and the fit of the SCPs without the peaks; in red we plotted the fit of the peaks, obtained with a gaussian ( $G(x)$ ). Bottom panels: same as the first ones, with added in red the total fit of the SCPs (polynomial for the bkg + gaussian for the peaks,  $f(x) + G(x)$ ).

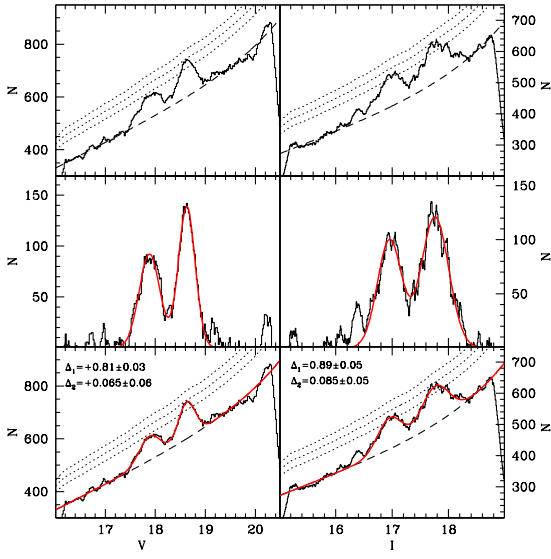


FIG. 8.— As Fig. 7, but for a different field (field F5A). The method is the same although this field shows more than one peak.

our detections with one of the N-body models of the tidal disruption of Sgr by Law et al. (2005). In particular we plot in Fig. 11 the results of the evolution of the N-body model of Sgr within a Galactic DM halo of prolate shape (flatness  $q=1.25$ , see Law et al. 2005; Johnston et al. 2005, for further details on the models). To compare observations and model in a consistent way we transformed our relative distances into absolute values by adopting the same distance modulus for Sgr as Law et al. (2005), i.e.  $(m - M)_0 = 16.9$  (Mateo et al. 1995a). The points of the model that are encountered by the considered F.o.V.s

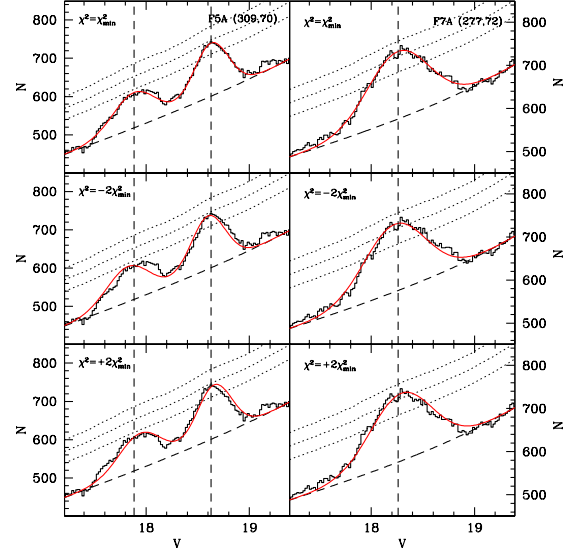


FIG. 9.— Upper panels: de-reddened running histogram SCPs, zoomed in the region of the peak(s), of color-selected RC candidates for the Stream field F5A (left panel) and F7A (right panel). The meaning of the lines is the same as Fig. 7, the red line represents the global model,  $f(x) + G(x)$ , with the best fit value of  $G(x)$  mean (value for which  $\chi^2 = \chi^2_{min}$ ). Middle and lower panels: as upper ones, with the exception that the values of the  $G(x)$  means are those that have  $\chi^2 = \pm \chi^2_{min}$  ( $\chi^2 = -2\chi^2_{min}$ , middle panels and  $\chi^2 = +2\chi^2_{min}$ , lower panels, respectively). It is clearly visible that in these last two cases the fit is totally unsatisfactory.

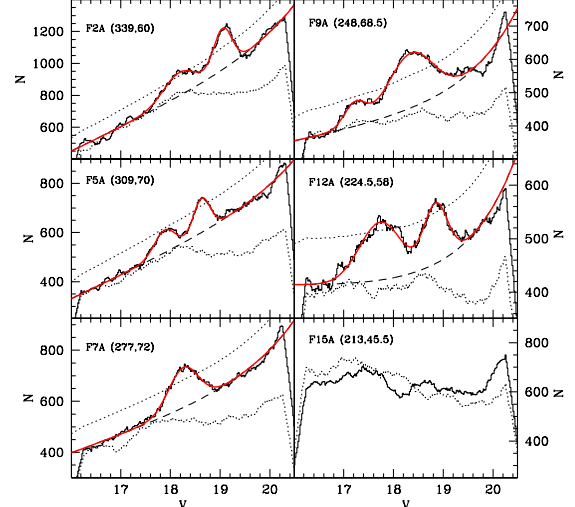


FIG. 10.— Comparison between a sample of the on-Stream SCPs studied in this paper (continuous histogram; best-fit model in red) and the SCP of the corresponding Control Fields.

along the *los* (F7A and F5A, from left to right, respectively) are plotted as heavier dots.

Taking the considered model as a realistic representation of the actual Sgr relic (a very reasonable assumption, in first approximation; Law et al. 2005), it is clear that any *los* around the considered plane would cross one or more different wraps of the Stream, at different distances (see Fig. 11). The peak from F7A and the most distant peak from F5A seem to match a distant portion of the leading arm. The nearest peak from F5A matches very well with a wrap of the trailing arm that appears narrow and well defined and that is crossed nearly perpendicular by the considered *los*. According to the considered

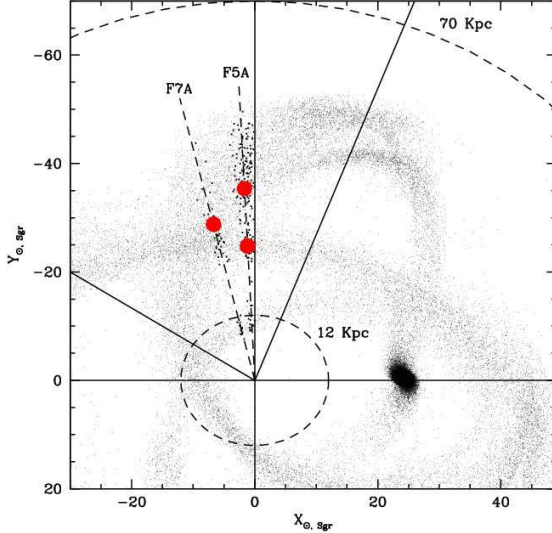


FIG. 11.— N-body model of the tidal disruption of Sgr by Law et al. (2005, prolate Dark Matter halo case) in heliocentric Sgr coordinates (see Majewski et al. 2003). The heavily printed dots are the subset of the model particles that are enclosed in the two observed fields considered here (F5A and F7A). The observed positions of the Stream in these fields, as estimated from the position of the RC peaks in our SCPs, are plotted as filled (red) circles.

model, both *los* should also cross a nearby wrap at a distance not enclosed in our range of sensitivity, that is delimited by the two dashed circles in Fig. 11. No wrap is expected to lie outside  $D=60$  kpc in the region sampled by our fields.

Both the more distant F5A detection and the single F7A detection occur in regions where the model predicts the confluence and crossing of different wraps. At a first glance to Fig. 11, it may appear that the constraining power of a single “mean position” of a Stream wrap, as derived with our method, is not sufficient to describe the complex structure of the Sgr remnant along a given *los*. In Fig. 12 we compare the observed RC peaks of F5A and F7A (and their best-fit gaussian models) with the peaks derived from the N-body model shown in Fig. 11 and from the oblate-halo model from the same set (Law et al. 2005) by (a) selecting the model particles encountered by the FoV cone, (b) assigning to each of them the absolute magnitude of the RC ( $M_V^{RC} = +0.72$  and  $M_I^{RC} = -0.23$ , according to Sect. 3) and deriving their apparent magnitude according to their distance, (c) adding gaussian photometric errors as a function of the apparent magnitude similar to the observed ones, and (d) producing the running histogram of the derived magnitudes with the same settings adopted for the observed SCPs. To make easier the comparisons shown in Fig. 12, the synthetic SCPs have been multiplied by an arbitrary normalization factor. The qualitative resemblance of the observed and predicted structures for the prolate-halo model is striking. On the other hand the oblate-halo model is clearly unable to reproduce the observations, even in terms of number of Stream wraps encountered by the considered *los*.

A more thorough comparison of our observations with theoretical models of the disruption of Sgr will be presented in Sect. 6. Here we are just interested to demonstrate that our method allows a detailed comparison between models and observations not only in terms of mean

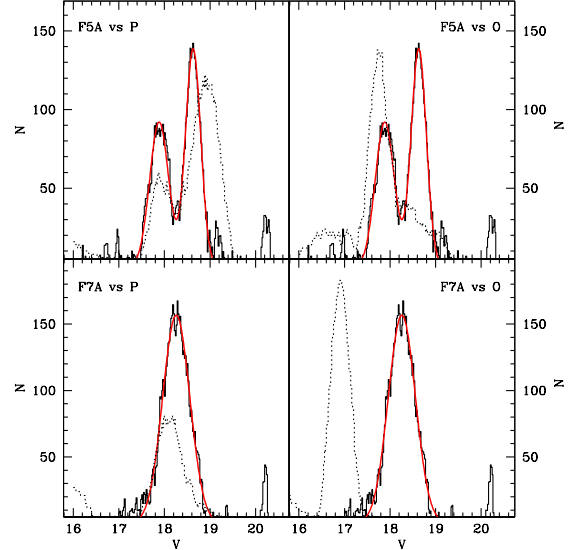


FIG. 12.— Comparison between the observed field-subtracted RC SCPs from F5A (upper panels) and F7A (lower panels) and the predictions of the N-body models by Law et al. (2005) in the same directions (left panels: prolate-halo model, the same as Fig. 11; right panels: oblate halo model). The observed SCPs are the continuous running histograms, the red continuous curves are the best-fit gaussians, the dotted running histograms are the predictions of the models, including the photometric errors. The histograms from the N-body models have been multiplied by arbitrary normalization factors (2 $\times$  and 3 $\times$ , for the left and right panels, respectively) to make the plots more readable.

distances, but also in terms of the actual *shape* of the structures along the *los* (see Fig. 12, left panels, in particular). In other words a fully successful model of the Sgr Stream must reproduce the correct position *and shape* of the observed peaks: this provides the opportunity for a fruitful detailed comparison between models and observations also in regions where different Stream wraps cross each other. In the present study we provide the position and the FWHM of the peaks (as the most basic shape parameter, see Sect. 3.5) but anyone interested in more detailed comparisons can easily reproduce our results and obtain plots like Fig. 12.

In Sect. 4 the SCPs of all the considered on-Stream fields, with the associated detections will be presented and briefly discussed. In agreement with the qualitative predictions of the model shown in Fig. 11, in most cases we will detect two peaks at different distances.

### 3.3. Classification of the detections

We divided the detections in three categories, assigning a *flag* to each of them, according to the following criteria:

- *flag* = 1: peaks that are above the  $3\sigma$  threshold both in the *V* and *I* SCPs, and having the same  $\Delta(Mag)$  in both passbands, within the errors. These are called *primary* peaks.
- *flag* = 2: peaks having the same  $\Delta(Mag)$  in both passbands, within the errors, but reaching the  $3\sigma$  threshold only in one of the two SCPs. In all the *flag* = 2 cases described in the following, the weaker peak is always just below  $3\sigma$ . These are called *secondary* peaks.
- *flag* = 3: clearly visible peaks having the same  $\Delta(Mag)$  in both passbands, within the errors, but

not reaching the  $3\sigma$  threshold in both the SCPs. These correspond to uncertain detections that we report just for completeness. In some case a weak peak in the SCP in one band is tentatively identified as it corresponds to a stronger peak in the other SCP. These peaks are called also *tertiary* peaks.

The observed SCPs and the detected peaks will be briefly described and discussed in Sect. 4.

#### 3.4. Number of RC stars associated to each peak

Our modeling of the observed SCP automatically provides also an estimate of the total number of stars associated to any given peak. This gives a useful additional constraint for theoretical models; we will illustrate this possibility with an example in Sect. 6.2. In Tab. 2 we provide the number of stars associated with a given peak normalized to an area of  $25 \text{ deg}^2$  (quite similar to the actual area of our fields). This number is the weighted mean of the estimates obtained from the  $V$  and  $I$  SCPs, where the assumed error on the estimate from each SCP is just the square root of the observed number (hence it should be considered as a lower limit to the real error).

Adopting the *Sgr34* field as a baseline (having  $N_{Sgr34}^{RC} \simeq 1500 \text{ stars}/\text{deg}^2$ , and  $mu_V \simeq 25.5 \text{ mag}/\text{arcsec}^2$ ; Monaco et al. 2005b), and translating our on-Stream estimates into stars/ $\text{deg}^2$  units ( $N_i^{RC}$ , for the field  $i$ ) we can transform our numbers into surface brightness, according to the same formula used in Bellazzini et al. (2006b):

$$\mu_{V,i} = \mu_{V,Sgr34} - 2.5 \log\left(\frac{N_i^{RC}}{N_{Sgr34}^{RC}}\right) + \Delta(m - M)_0 \quad (4)$$

derived from Renzini (1998), where  $\Delta(m - M)_0 = (m - M)_0^i - (m - M)_0^{Sgr34} = \Delta V = \Delta I$ . Using the equation 4 we find that the  $V$  surface brightness of the portions of the Sgr Stream studied in the present paper range between  $30.6 \text{ mag}/\text{arcsec}^2$  and  $33.6 \text{ mag}/\text{arcsec}^2$ , quite typical of tidal tails and in good agreement with previous results (see, for example, Bellazzini et al. 2003b, and references therein).

It is important to recall that the measured densities refer only to RC stars: in the presence of a population gradient (as is likely the case in the Stream, Bellazzini et al. 2006c; Chou et al. 2007) they would trace different fractions of the total stellar content at different positions along the Stream. Analogously, the derived surface brightness estimates have been rescaled assuming the stellar mix of *Sgr34* for all the considered portions of the Stream. For this reason these estimates should be considered with caution: given the sense of the gradient it is expected that they provide lower (faint) limits when converted into luminosity or surface brightness. In this context, it is interesting to note that if we convert our surface brightness into the same density units ( $L_\odot/\text{kpc}$ ) adopted by Niederste-Ostholt et al. (2010), we find that our results are fully compatible with the trend of density as a function of RA derived by these authors (see their Fig. 7), for both branches. On the other hand, our densities are lower than theirs by a factor of  $\sim 4 - 5$ . It is reasonable to assume that part of the difference may be accounted for by the effect of the population gradient described above.

#### 3.5. Depth along the los of the Stream wraps

Fig. 12 shows that the observed RC peaks contain also valuable information on the characteristic size of the section of the Stream branches crossed by our *los*, as peaks at similar distances display different widths. To obtain a quantitative estimate of the linear width along the *los* of the structures identified here, we recurred to the synthetic population described in Sect. 2.3. In particular we tried to reproduce the *models* of the observed peaks<sup>14</sup> with smoothed histograms of the synthetic RC population, properly including the effects of photometric errors. As done in Sect. 2.3, we assign a distance along the *los* to each star of the synthetic RC population according to a gaussian distribution having the same mean and normalization as the observed peak, and we search for the value of  $\sigma_d$  giving the best match between the two models. In Tab. 2 we report the Full Width at Half Maximum (in kpc) of the adopted distributions,  $\text{FWHM} = 2.35\sigma_d$ . The best match is found by minimizing  $\chi^2$ , typical uncertainties are  $\sim 20\%$ . The adopted procedure gets rid of the effects of the distance on the width of the SCP peaks discussed in Sect. 2.3.

Since the synthetic population that we adopt is strictly single-age and single-metallicity, the intrinsic luminosity width of its RC should be smaller than the actual width of the RC of Sgr, as the latter hosts stars spanning a range of ages and metallicities (B06a, Girardi & Salaris 2001; Siegel et al. 2007; Bellazzini et al. 2008). For this reason the FWHM values we obtain in this way must be considered as strong *upper limits* to the real values. Moreover, it has to be recalled that we report FWHM along a given *los*, that may have various incidence angles with respect to the encountered Stream wraps. Applying the method to the *Sgr34* field we obtain  $\text{FWHM} \simeq 3 \text{ kpc}$ , not too far from the minor-axis FWHM in the plane of the sky as obtained from the best-fit King (1962) model by Majewski et al. (2003), i.e.  $\text{FWHM} \simeq 1.1 \text{ kpc}$ , in particular if we take into account that the *los* toward the core of Sgr is (likely) not exactly perpendicular to the major axis of the dwarf galaxy (see Fig. 11). Based on this test, it is reasonable to assume that our FWHM overestimates the true values by a factor of  $\gtrsim 2$ .

In any case, the ratio between the FWHM of two different *los* /locations in the Stream, or, equivalently, the differential trend of the FWHM as a function of orbital azimuth along a given Stream wrap, can be directly compared to the predictions of theoretical models of the disruption of Sgr.

#### 4. ON-STREAM DETECTIONS

In this section we present all the SCPs obtained from each analyzed field of branches A and B; we plot the SCPs in the  $V$ - and  $I$ -bands in Fig. 15 for branch A, and Fig. 16 for branch B. Together with the observed SCPs, we plot also the background model ( $f(x)$ , dashed lines), the threshold limits for the detections (dotted lines, respectively  $3, 4, 5\sigma$ ), which as mentioned previously, include both the Poisson noise and the uncertainty in the

<sup>14</sup> In this way we avoid any problem associated with the (partial) overlap of *observed* peaks; adjacent overlapping peaks are disentangled by our models as Point Spread Function -fitting photometric packages disentangle the fluxes from two partially overlapping stars on an image.

fit, and the global model that fits the observed SCPs ( $f(x) + G(x)$ , red lines). Each field is labeled according to the names assigned in Table 1 and with its Galactic coordinates (l,b).

In summary, we detect 26 *primary* (flag=1) peaks, 10 *secondary* (flag=2), and 14 *tertiary* (flag=3) peaks. Most of the considered SCPs show two significant peaks, corresponding to subsequent crossings of different wraps of the Stream along the *los*. The trend of peak distance as a function of Sgr longitude ( $\Lambda_{Sgr}$ ) shown in Fig. 13 can be useful to better understand the morphology of the various SCPs presented below. Most primary peaks appear to trace a wrap of the leading arm whose distance from the Sun steadily decreases from  $D \simeq 45$  kpc at  $\Lambda_{Sgr} \simeq 290^\circ$  to  $D \simeq 20$  kpc at  $\Lambda_{Sgr} \simeq 230^\circ$ . Both primary and secondary peaks trace a more nearby filamentary structure at constant distance  $D \simeq 25$  kpc, from  $\Lambda_{Sgr} \simeq 290^\circ$  to  $\Lambda_{Sgr} \simeq 260^\circ$ , that then bends toward larger distances, reaching  $D \simeq 40$  kpc at  $\Lambda_{Sgr} \simeq 230^\circ$ . This feature is tentatively identified as a wrap of the trailing arm (see Sect. 6). The two wraps cross at  $\Lambda_{Sgr} \sim 245^\circ$  (see Sect. 6). Some secondary and tertiary peaks seem to trace more feeble distant or nearby wraps (see Sect. 6 for a deeper discussion). The comparison with the considered model suggests that most of the detected peaks can be associated with the Sgr Stream. The tertiary peak at  $\Lambda_{Sgr} \sim 263^\circ$  and  $D \simeq 18$  kpc, and the primary peak at  $\Lambda_{Sgr} \sim 280^\circ$  and  $D \simeq 19.5$  kpc, are possibly associated to other overdensities in the Virgo constellation (see Jurić et al. 2008; Duffau et al. 2006; Newberg et al. 2007, and references therein), as discussed in some detail in Sect. 6.

Before proceeding in the description of the various detections, we anticipate that the differential distance moduli ( $\Delta V = V_{RC}^{Field} - V_{RC}^{Sgr}$ <sup>34</sup>; the analogous definition being valid also for  $\Delta I$ ), reported in Tab. 2, obtained from primary and secondary peaks detected in the  $V$  and  $I$  SCPs are in *excellent* agreement, as shown in Fig. 14. This confirms the reliability of our detections and distance estimates. For this reason, from Sect. 5 on and in Fig. 13 we adopt the mean of  $\Delta V$  and  $\Delta I$  as our final differential distance moduli estimates.

#### 4.1. Branch A detections

In branch A we analyzed 15 fields, the corresponding observed SCPs and the adopted best-fit models are shown in Fig. 15. We obtained a total of 24 peak detections, with the following classification: 10 primary peaks, 5 secondary peaks and 9 tertiary peaks. The SCPs of the first five fields (from F1A to F5A, upper left panel and first two rows of the upper right panel of Fig. 15) display a common general behaviour: they present two main peaks, the one at fainter magnitudes always being the strongest (a *primary* peak in all cases), while the brighter ones are wider and span all the classes from flag=1 to flag=3, depending on the specific field. It is quite clear that this series of peaks traces two coherent structures placed at different distances along the *los*. The  $I$ -band SCP of F4A may suggest a splitting of the brighter/weaker peak into two separate components: we consider this interpretation as unlikely, nevertheless the result obtained with a three peaks model is briefly discussed in Sect. 4.3. The only exception is a primary peak detected at  $V \sim 16.5$  in F1A: this likely corresponds to

the nearest wrap of the Stream that emerges from the  $d \lesssim 12$  kpc circle (where our method is blind), which is the most Eastern of all the considered *los* (see Sect. 6).

The SCPs of F6A (second upper right panel of Fig. 15) present an overall structure similar to those described above. However we identified additional (fainter) peaks, and finally we adopted a three peak solution, whose validity is confirmed by the inspection of SCPs obtained with reduced bin width (i.e., higher resolution<sup>15</sup>; see Sect. 4.3 for an alternative). The newly-resolved third peak, at magnitude  $V \sim 19$  ( $I \sim 18$ ), corresponds to a distance  $D \simeq 42$  kpc at  $\Lambda_{Sgr} \simeq 265^\circ$ ; this detection seems related to a very distant wrap of the leading arm (see for example Fig. 22). F6A is the only branch-A field in which we detect a peak related to this distant wrap of the leading arm, that was observed also by Bel06 (see Sect. 5); the same structure is detected in branch B along the same *los*, as well as along an additional one (F8B).

F7A is one of two fields in branch A that presents only one detection: SCPs (third upper right panels of Fig. 15) show a single, very prominent *primary* peak. As discussed above, this *los* intercepts a region where two or three wraps of the Stream cross each other. Fig. 12 shows that the presence of a single peak is nevertheless consistent with model predictions. In both the SCPs of the adjacent field F8A, a remarkably weak peak appears at similar position as in F7A, hence we obtain only a tentative flag=3 detection. We have no convincing explanation for the weakness of the peak detected in this field: it may be related to the complex structure of the various Stream wraps or to a local dip in the density along the Stream. However, the derived distance is in good agreement with the trend observed in others Branch-A fields. In the SCPs of F9A field we identify again two peaks, the faintest one being very prominent and wide; also this *los* intercepts a region of crossing wraps, thus superposed structures may contribute to the production of a strong and remarkably wide primary peak. The weaker/brighter peak is more interesting: it is clearly identified in both SCPs, even if below the  $3\sigma$  threshold, at  $V \sim 17.20$  ( $I \sim 16.30$ ): as discussed later in Sect. 6 this feature may trace a near wrap of the Stream that was never detected before.

SCPs of fields from F10A to F12A show two peaks at similar positions, with a remarkable variety of absolute and relative strengths. This may reflect the highly structured morphology that is suggested by models in this region (see Sect. 6). F11A is crossed by the Orphan Stream (Bel06, Belokurov et al. 2007). While the distance of this structure ( $\sim 30$  kpc toward this *los*) does not match with the detected peaks we cannot rule out some contamination from Orphan Stream stars in this field.

We did not find any convincing signal in F13A, F14A and F15A; the overall shape of the SCPs appear quite different from the other cases and, in the case of F15A, the polynomial model did not provide a satisfactory fit to the background population. In particular, the SCPs present a strong excess at bright magnitudes ( $V \lesssim 18$ ,  $I \lesssim 17$ ) with respect to those in the previously-discussed fields, such that they appear flat or even decreasing with

<sup>15</sup> We note that this is the only case in which a change in the bin width produced a change in the interpretation of the SCPs.

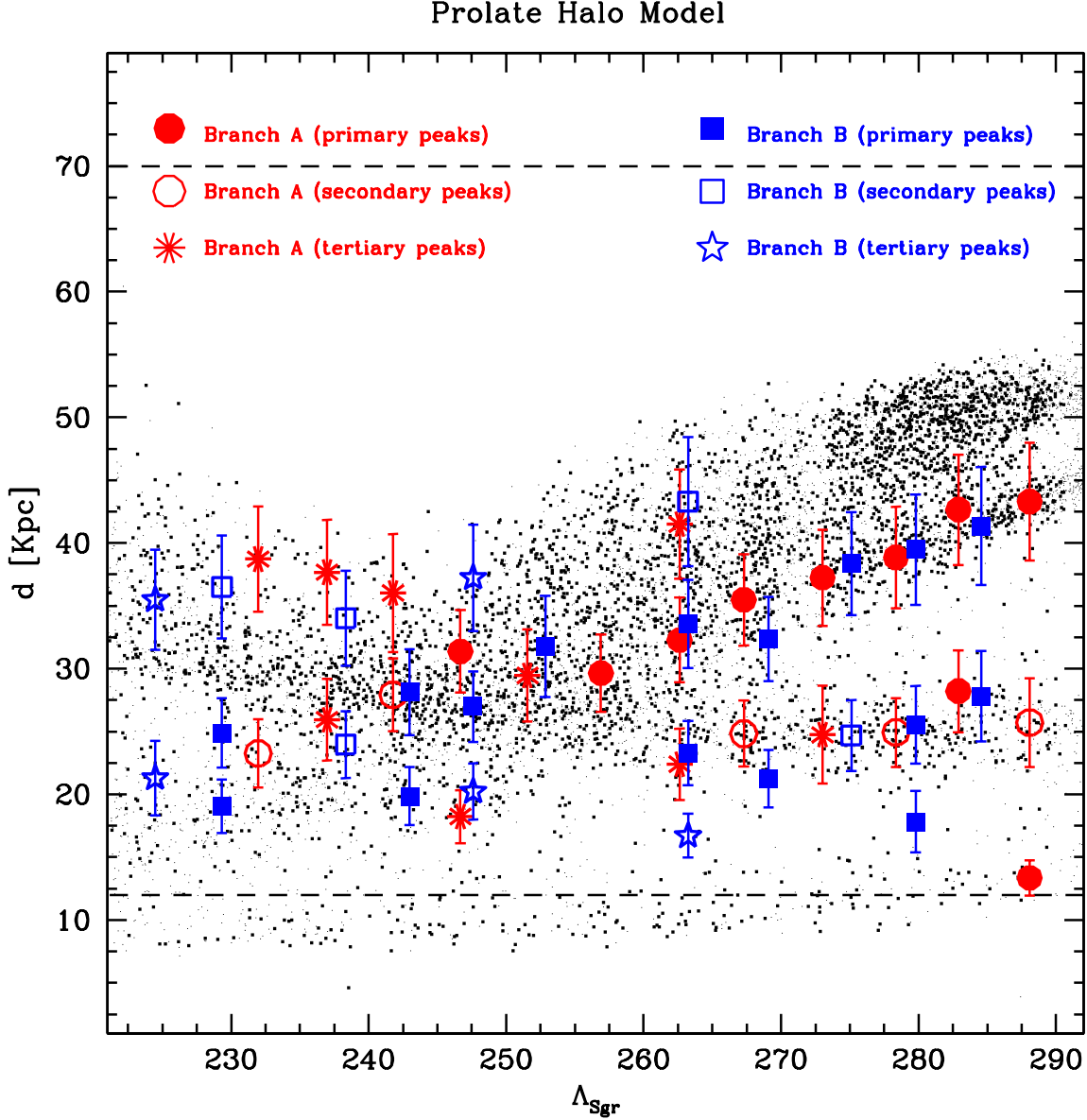


FIG. 13.— Distribution of the *primary* (red filled circles - branch A -, and blue filled squares - branch B), *secondary* (red open circles - branch A -, and blue open squares - branch B) and *tertiary* detections (red starred symbols - branch A, and blue stars - branch B) in the  $\Lambda_{Sgr}$  vs. heliocentric distance plane (a true distance modulus of 16.90 has been adopted here). The horizontal dashed lines enclose the range of sensitivity of our method. The prolate-halo N-body model by Law et al. (2005) is also reported (small dots) as an aid for the interpretation of the plot. The heavier dots are those enclosed in the cones of the considered FoVs.

increasing magnitude. These are the fields at the lowest galactic latitude, hence we attribute these features to contamination by (relatively) nearby stars from the Galactic thick disk (and, possibly, the Monoceros structure, see Fig. 1 of Bel06) that overwhelms the signal from the Sgr Stream RC. This seems confirmed by the comparison with the corresponding CFs (the case of F15A is shown in Fig. 10, in Sect. 3.1), that display SCPs essentially indistinguishable from those of the on-Stream fields. This implies that the adopted technique can be used successfully only at large distances from the Galactic plane. Given the above reasons we preferred not to consider for further analysis the possible peaks at  $V(I) \sim 16(15)$  and  $V(I) \sim 17.5(16.5)$  in F14A.

#### 4.2. Branch B detections

In branch B we analyzed 13 fields, obtaining a total number of 26 detections, with the following classification: 16 primary, 5 secondary and 5 tertiary peaks. The main structures found in branch A are mirrored also in branch B, as clearly shown in Fig. 13. In all the fields (except F7B) we detect at least two peaks; in two cases (F8B and F12B) we also detect a third peak; in F8B this is likely tracing the more distant Stream wrap running nearly parallel to the main wrap of the leading arm (see above and Fig. 13); in another case (F5B), in addition to three peaks analogous to those in F8B, we found an additional nearby peak (see Sect. 6 for a discussion). An alternative interpretation for the SCPs of F12B is presented in Sect. 4.3. Quite surprisingly, the SCPs of F6B appear completely smooth and featureless. In this case we were not able to find an explanation for this behavior (but see above for the discussion of the similar case of

TABLE 2  
DISTANCE, FWHM AND DENSITY FOR THE DETECTED RC PEAKS.

field	$l^\circ$ deg	$b^\circ$ deg	$\Delta V$ mag	$\epsilon \Delta V$ mag	$\Delta I$ mag	$\epsilon \Delta I$ mag	d kpc	$\epsilon d$ kpc	sign. (V)	sign. (I)	FWHM kpc	$N_{RC}$ [stars/25 deg $^2$ ]	$\epsilon N$ [stars/25 deg $^2$ ]	flag 1
1A	346	56	1.28	0.07	1.28	0.06	47.5	5.1	$\geq 5\sigma$	$5\sigma$	9.8	241	11	1
			0.21	0.14	0.08	0.15	28.2	3.9	$4\sigma$	$< 3\sigma$	7.1	353	9	2
			-1.27	0.05	-1.27	0.05	14.6	1.1	$3\sigma$	$3\sigma$	1.3	79	6	1
2A	339	60	1.23	0.05	1.27	0.04	46.8	4.8	$\geq 5\sigma$	$\geq 5\sigma$	4.2	227	9	1
			0.36	0.09	0.34	0.09	30.9	3.6	$4\sigma$	$3\sigma$	9.5	303	10	1
3A	331	63	1.04	0.04	1.05	0.05	42.6	4.4	$> 5\sigma$	$\geq 5\sigma$	11.3	345	13	1
			0.06	0.07	0.00	0.09	26.6	3.0	$4\sigma$	$< 3\sigma$	6.2	327	10	2
4A	320	66	0.94	0.04	0.97	0.05	40.8	4.2	$\geq 5\sigma$	$5\sigma$	7.5	158	8	1
			0.08	0.09	0.05	0.15	27.1	4.3	$< 3\sigma$	$< 3\sigma$	14.6	226	10	3
5A	309	70	0.81	0.03	0.89	0.05	38.9	4.0	$4\sigma$	$4\sigma$	8.6	114	8	1
			0.06	0.06	0.08	0.05	27.2	2.9	$< 3\sigma$	$> 3\sigma$	5.1	116	7	2
6A	296	72	0.62	0.04	0.67	0.06	36.0	3.8	$4\sigma$	$4\sigma$	7.0	171	11	1
			-0.08	0.12	-0.22	0.12	24.6	3.1	$< 3\sigma$	$< 3\sigma$	3.9	66	7	3
			1.18	0.05	1.20	0.05	45.5	4.8	$< 3\sigma$	$< 3\sigma$	1.4	49	6	3
7A	277	72	0.44	0.04	0.48	0.06	32.5	3.4	$\geq 4\sigma$	$\geq 4\sigma$	10.9	188	10	1
8A	260	71.5	0.53	0.10	0.36	0.13	32.3	4.0	$< 3\sigma$	$< 3\sigma$	3.9	122	6	3
9A	248	68.5	0.53	0.05	0.63	0.05	34.4	3.6	$5\sigma$	$5\sigma$	17.0	231	10	1
			-0.59	0.08	-0.59	0.10	20.0	2.3	$< 3\sigma$	$< 3\sigma$	2.6	71	6	3
10A	238	65.5	0.33	0.06	0.33	0.04	30.6	3.2	$3\sigma$	$< 3\sigma$	5.3	90	5	2
			0.94	0.15	0.84	0.10	39.5	5.1	$< 3\sigma$	$< 3\sigma$	3.0	64	4	3
11A	230.5	62	0.93	0.08	1.03	0.07	41.3	4.6	$< 3\sigma$	$< 3\sigma$	9.5	42	6	3
			0.15	0.15	0.18	0.07	28.4	3.6	$< 3\sigma$	$< 3\sigma$	6.2	37	5	3
12A	224.5	58	1.03	0.06	1.05	0.07	42.5	4.6	$> 3\sigma$	$< 3\sigma$	4.2	103	7	3
			-0.08	0.09	-0.05	0.10	25.5	3.0	$> 3\sigma$	$3\sigma$	9.8	167	10	2
1B	353	61	1.16	0.08	1.20	0.09	45.3	5.2	$3\sigma$	$3\sigma$	6.9	172	8	1
			0.32	0.10	0.32	0.15	30.5	3.9	$3\sigma$	$3\sigma$	12.5	352	11	1
2B	346.5	65	1.08	0.09	1.08	0.06	43.3	4.8	$\geq 5\sigma$	$\geq 5\sigma$	9.3	187	10	1
			0.18	0.12	0.09	0.09	28.0	3.4	$5\sigma$	$5\sigma$	8.8	374	11	1
			-0.65	0.14	-0.64	0.15	19.5	2.7	$3\sigma$	$3\sigma$	3.5	124	8	1
3B	337.5	68.5	1.01	0.07	1.03	0.05	42.1	4.5	$> 3\sigma$	$> 3\sigma$	6.8	234	8	1
			0.05	0.08	0.07	0.09	27.1	3.1	$3\sigma$	$< 3\sigma$	6.8	170	8	2
4B	329.5	74	0.60	0.05	0.70	0.05	35.5	3.7	$> 5\sigma$	$5\sigma$	15.0	271	11	1
			-0.24	0.05	-0.28	0.07	23.3	2.5	$> 4\sigma$	$3\sigma$	3.1	160	6	1
5B	313.5	78.5	0.73	0.05	0.73	0.05	36.8	3.8	$5\sigma$	$5\sigma$	6.5	125	7	1
			-0.08	0.07	-0.05	0.07	25.5	2.8	$4\sigma$	$3\sigma$	4.1	133	7	1
			1.38	0.10	1.18	0.10	47.5	5.5	$< 3\sigma$	$> 3\sigma$	6.9	56	7	2
			-0.80	0.05	-0.77	0.05	18.3	1.9	$< 3\sigma$	$< 3\sigma$	2.2	61	5	3
7B	256	80	0.66	0.10	0.56	0.14	34.8	4.4	$3\sigma$	$> 3\sigma$	$\sim 20.0$	201	10	1
8B	234	77	0.25	0.05	0.26	0.05	29.6	3.1	$4\sigma$	$> 4\sigma$	6.5	115	7	1
			-0.34	0.07	-0.40	0.08	22.2	2.5	$< 3\sigma$	$< 3\sigma$	3.3	93	5	3
			0.93	0.08	0.98	0.09	40.8	4.6	$< 3\sigma$	$< 3\sigma$	9.2	89	7	3
9B	224	73	0.41	0.09	0.28	0.12	30.8	3.7	$\geq 3\sigma$	$3\sigma$	12.0	190	8	1
			-0.44	0.07	-0.37	0.11	21.8	2.5	$> 3\sigma$	$3\sigma$	3.1	59	6	1
10B	216.5	69	0.76	0.10	0.75	0.04	37.3	4.1	$< 3\sigma$	$> 3\sigma$	7.0	111	8	2
			0.02	0.102	-0.02	0.04	26.3	2.9	$< 3\sigma$	$> 3\sigma$	4.4	74	8	2
12B	208.5	60.5	0.88	0.15	0.94	0.15	40.0	5.6	$< 3\sigma$	$3\sigma$	8.1	92	6	2
			0.07	0.08	0.09	0.07	27.3	3.0	$3\sigma$	$3\sigma$	4.0	79	6	1
			-0.50	0.07	-0.50	0.08	20.9	2.3	$3\sigma$	$3\sigma$	2.4	75	6	1
13B	203	56.5	0.89	0.08	0.81	0.08	38.9	4.4	$< 3\sigma$	$< 3\sigma$	7.2	81	6	3
			-0.20	0.15	-0.32	0.15	23.3	3.2	$< 3\sigma$	$< 3\sigma$	6.7	142	6	3

F8A).

In analogy with F7A (and F8A) F7B is the only case of branch B SCPs fitted with a single peak model. The morphology of the  $I$ -band SCP and the comparison with the adjacent F8B field suggest that two, or possibly three peaks may be merged together in this SCP. However we were unable to resolve the peak into separate components even in SCPs with smaller bin width (as for the case of F6A). We caution the reader that this primary detection is likely concealing significant — but as yet undetected — substructure.

### 4.3. A few special cases

There are a few cases in which the observed SCPs do not provide unequivocal indications for the model to be adopted, in particular concerning the number of  $G_i(x)$  functions to be included in the model, i.e. the number of detected peaks. F7B, briefly discussed above, is the only case in which we feel that the observed peak is due to the merging of two (or, more likely, three) adjacent peaks that we cannot resolve. In Fig. 17 we present acceptable

alternative models (with respect to the solutions shown in Figs. 15 and 16, and listed in Tab. 2) for the three cases in which our preference for the adopted models (Tab. 2) is only marginal, and is also supported by the continuity within a large scale structure (a Stream wrap). In Tab. 3 we report the corresponding alternative solutions, that can be replaced with those of Tab. 2 by those readers who may use our values to constrain models of Sgr, if they judge them more appropriate, for some reason.

### 4.4. Intra-Branch fields

In the present analysis we do not consider the structure of the Stream in the Dec direction. We fully adopted the view of Belokurov et al. (2006), where the leading arm of the Stream as seen from TO stars in the SDSS bifurcates into branch A and branch B around RA=220° and the separation between the branches increases with decreasing RA. We proceeded to a basic verification of this scenario by looking at the SCPs of a few Intra-Branch (I) fields (not shown here, for brevity), located at intermediate Dec with respect to the A and B fields F5, F7,

TABLE 3  
ALTERNATIVE SOLUTIONS FOR THREE *los* .

field	$l^{\circ}$ deg	$b^{\circ}$ deg	$\Delta V$ mag	$\epsilon \Delta V$ mag	$\Delta I$ mag	$\epsilon \Delta I$ mag	d kpc	$\epsilon d$ kpc	sign. (V)	sign. (I)	FWHM kpc	$N_{RC}$ [stars/25 deg $^2$ ]	$\epsilon N$ [stars/25 deg $^2$ ]	flag
4A	320	66	0.94	0.04	0.97	0.05	40.8	4.2	$\geq 5\sigma$	$5\sigma$	7.5	158	8	1
			0.28	0.07	0.36	0.10	30.5	3.5	$< 3\sigma$	$< 3\sigma$	3.2	119	7	3
			-0.16	0.09	-0.17	0.09	24.4	2.8	$< 3\sigma$	$< 3\sigma$	1.9	107	6	3
2B	346.5	65	1.08	0.09	1.08	0.06	43.3	4.8	$\geq 5\sigma$	$\geq 5\sigma$	9.3	187	10	1
			0.13	0.15	0.08	0.12	27.6	3.7	$5\sigma$	$5\sigma$	14.0	499	14	1
12B	208.5	60.5	0.88	0.15	0.94	0.15	40.0	5.6	$< 3\sigma$	$3\sigma$	8.1	92	6	2
			-0.21	0.15	-0.17	0.15	24.1	3.3	$3\sigma$	$3\sigma$	12.0	155	9	1

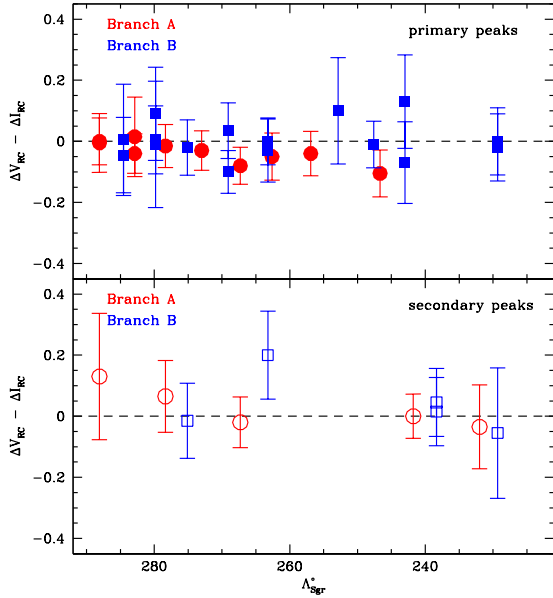


FIG. 14.— Comparison between the differential distance moduli obtained from peaks in the  $V$  and  $I$  SCPs for primary (upper panel) and secondary (lower panel) peaks.

F10 and F12. In agreement with the results of Belokurov et al. (2006), we find that the SCPs of F5I and F7I mimic the structure of the SCPs of the corresponding A and B fields, showing peaks at the same position and with similar shape, but weaker than in the on-Stream fields (i.e. tracing a lower stellar density). In the SCPs of F10I the peaks seen in the A and B SCPs are just barely visible and they completely disappear in F12I. Hence, these limited set of tests confirm the reality and the morphology of the Stream bifurcation as observed by Belokurov et al. (2006).

#### 4.5. The color of the RC peaks

The color of the RC peak is known to be very sensitive to metallicity and weakly sensitive to age, in the range of ages relevant for the present study (4-12 Gyr, Girardi & Salaris 2001). As our procedure of independent peak detections in  $V$ - and  $I$ -band SCPs automatically provides the colors of the RC peaks, it is worth checking if there is any hint of a color (metallicity) gradient along the Stream. In Fig. 18 the colors of the observed peaks are compared to the theoretical models by Girardi & Salaris (2001). All of the peak detections shown in Fig. 18 are compatible with having the same color within the uncertainties (that are quite large for some non-primary peaks). It is interesting to note that the large majority of points cluster around the  $[M/H] = -0.7$  model, in good agreement with the results by Bellazzini et al. (2006a)

and Carrell & Wilhelm (2010) (see also Sect. 2.1). No significant trend of color (metallicity) of the RC population with orbital azimuth is apparent and the few points showing the larger color difference from the mean locus are always among those having the most uncertain color estimates.

#### 5. COMPARISON WITH PREVIOUS ANALYSES

Before discussing in detail the comparison between our distance estimates and the findings from previous works, it is worth considering the difference between the performances of the various adopted tracers. The intrinsic stability (and ubiquity along the Stream) of our standard candle (RC stars), the adopted analysis, best suited for the detection and location of RC peaks, and the purely differential nature (Stream vs. main body) of our measures, make our distance estimates the most comprehensive, accurate and *homogeneous* set publicly available (even if limited to the region of sensitivity described above). The uncertainties associated with our estimates are lower than any previous work, with a typical values of  $\leq 5\%$ , raising to  $\leq 10\%$  in the worst cases. For example, Majewski et al. (2003) reports that the characteristic uncertainty of their photometric parallaxes based on M-giant is  $\simeq 20\%$ ; Martin et al. (2004) showed that uncertainties in the age/metallicity of the considered populations may lead to systematics of order  $\sim 30\%$  in the distance scale based on M giants. F stars (assumed to be TO stars of Sgr) proved to be an excellent mean to trace even very feeble substructures (Belokurov et al. 2006; Newberg et al. 2007). However the assumption of a common absolute magnitude for all color-selected F stars implies large uncertainties, as these stars span a range of luminosities much larger than RC stars. For example, if we consider the distribution in  $V$  magnitude of (a) the RC selected with our color window, and (b) the MSTO stars selected in color as done by Bel06 (and limited to  $V > 20.0$ ) in the photometry of the *Sgr34* field, we found two obvious single peaked distributions, but while the FWHM of the RC peak is  $\simeq 0.3$  mag, the MSTO star peak has  $FWHM \simeq 2$  mag. Indeed, Cole et al. (2008), in their pilot project on stripe 82, showed that the assumption of a fixed magnitude for these stars may lead to very large errors. Blue Horizontal Branch stars are easier to select against the Galactic fore/background, but are rarer than RC stars. Moreover, even if selected in a color range where the Horizontal Branch is really nearly horizontal, the distribution in magnitude of these stars is not expected to be as clearly peaked as the RC (see B06c). In this sense, the Sub Giant Branch (SGB), used by Bel06 and Keller (2009b), is more promising, as it is a very narrow feature in CMDs of metal rich populations. However it should be much more sensitive to metallicity

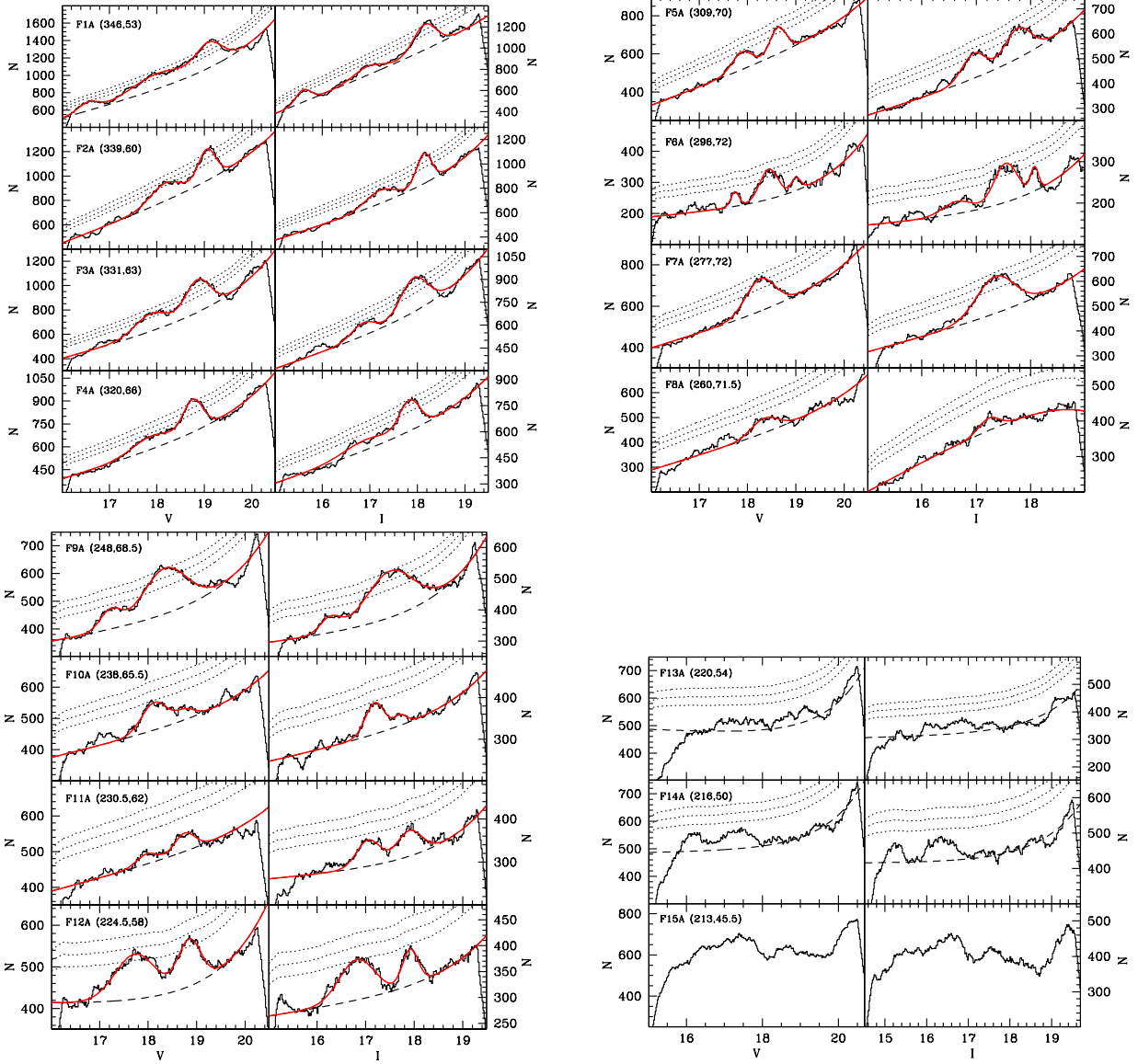


FIG. 15.— Fits of the observed SCPs (in  $V$  and  $I$ ) for fields on Branch A of the Sgr Stream. The numbers in parentheses are the Galactic longitude and latitude of the center of the field, in degrees. The meaning of the symbols is the same as in Figg. 7 and 8, above. No global fit has been attempted for SCPs that did not show significant RC peaks (F13A, F14A, F15A).

and age variations than the RC (see, for example, B06a, and references and discussion therein), and being much (intrinsically) fainter, its use is limited to a lower distance range, for any given dataset. Finally, RR Lyrae stars (Ivezić et al. 2000a; Vivas & Zinn 2006; Prior et al. 2009a; Keller et al. 2008) can provide distances with even superior accuracy with respect to our method; well sampled light curves can also give indications on physical properties of individual stars (metallicity, for example) that cannot be obtained from RC stars. However RR Lyrae are (likely) less frequent than RC stars over most of the Stream extension and, above all, they need time series information to be safely identified and to obtain a reliable apparent magnitude averaged over the pulsation period: for this reason the available data cover a much smaller region of the sky with respect to generic “single epoch” standard candles.

### 5.1. Comparison with specific detections

Yanny et al. (2000) were the first to interpret a stellar over-density in the halo as possibly due to the Sgr Stream. In the first available (equatorial) stripe of the SDSS they identified an excess of A-type stars around  $\Lambda_{\odot} \sim 295^{\circ}$ , adjacent to our field F1A. The heliocentric distance inferred is of 48 kpc, in good agreement with our estimate for the main wrap of the leading arm in this direction ( $D \simeq 45$  kpc at  $\Lambda_{Sgr} \simeq 290^{\circ}$ ). This result was later confirmed by the more thorough study by Newberg et al. (2002), that used F stars as main tracers. Although they do not comment on it, the Yanny et al. (2000) data also showed an excess of A-type stars less than 20 kpc away along the same  $los$  (see their Fig. 18 and 19). This may be more easily identified with the constant-distance coherent structure we see at  $d \simeq 25$  kpc than to the nearest wrap that we (possibly) detect at  $\Lambda \simeq 287^{\circ}$  and  $d \simeq 13$  kpc.

A similar detection of two density enhancements toward the Northern Loop was reported by Ivezić et al. (2000a), from the study of RR Lyrae in the same SDSS

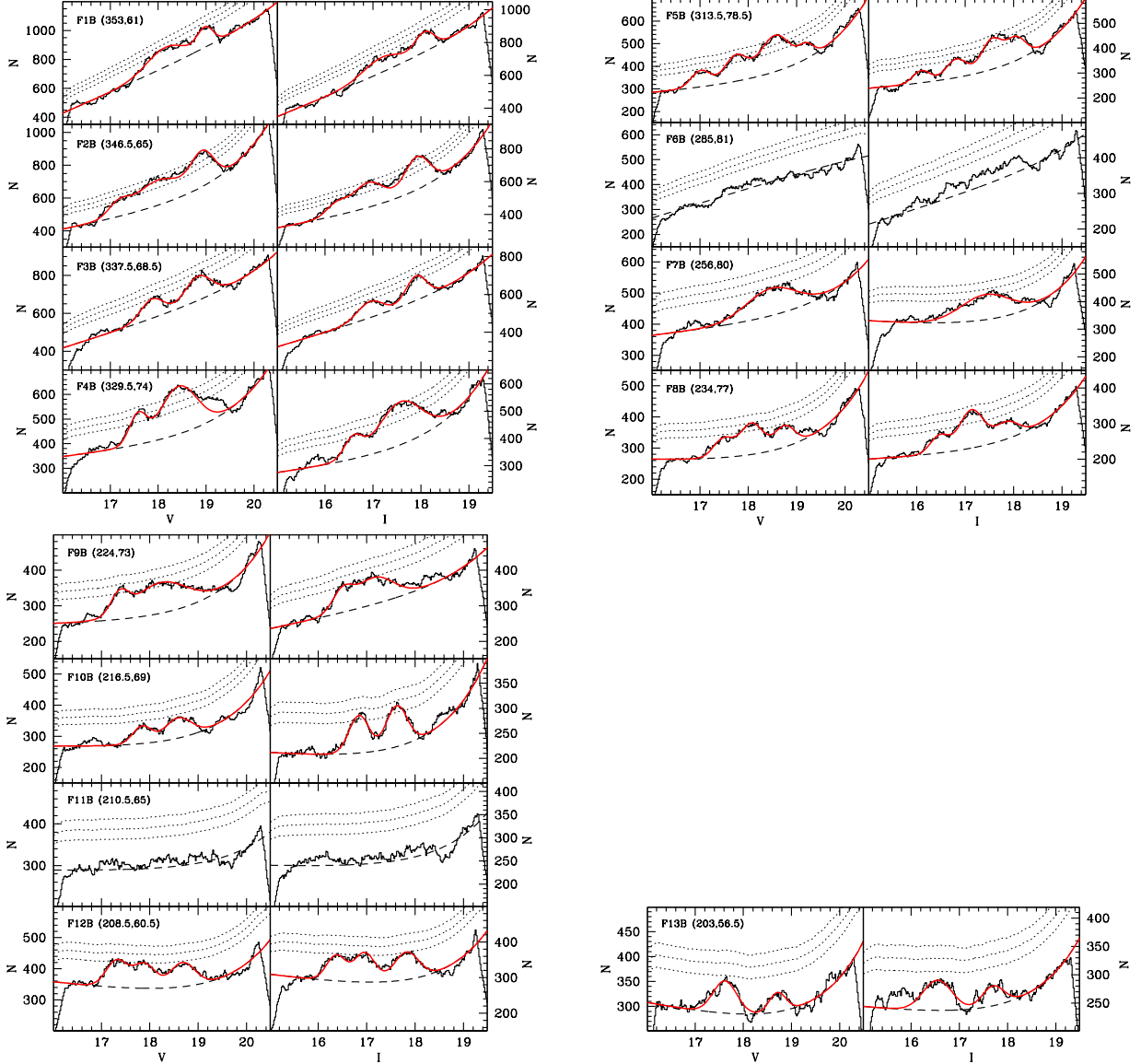


FIG. 16.— The same as Fig. 15 but for fields on Branch B of the Sgr Stream. No global fit has been attempted for SCPs that did not show significant RC peaks (F6B, F11B).

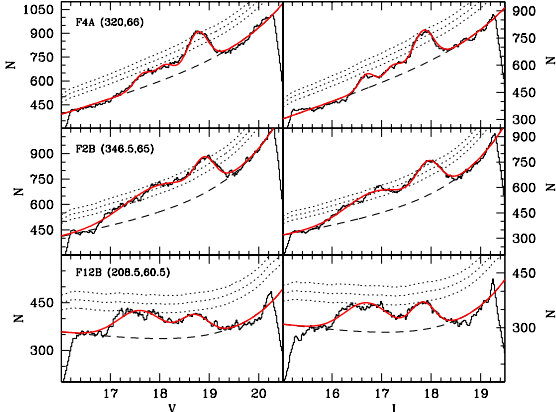


FIG. 17.— Fits of the observed SCPs (in  $V$  and  $I$ ) for fields of the branch A and B of Sgr Stream for which we present acceptable alternative models, with respect to the solutions shown in Figs. 15 and Figs. 16. The numbers in parentheses are the Galactic longitude and latitude of the center of the field, in degrees. The meaning of the symbols is the same as in Figs. 7 and 8, above.

stripe studied by Yanny et al. (2000), and by Vivas & Zinn (2006), also using RR Lyrae from the QUEST RR survey, which explored nearly the same region of sky ( $\Lambda_{\odot} \sim 270^\circ - 290^\circ$ ). Both studies comment primarily on an excess of RR Lyrae stars at 45-50 kpc (corresponding to the main wrap of the leading arm); however a structure around  $\sim 20$  kpc is also noted.

Majewski et al. (2003), provided a clear panoramic view of the Sgr Stream using M giants as standard candles; they were able to trace very neatly the trailing tail all over the Southern Galactic hemisphere, as well as part of the leading arm closer to the main body of the galaxy, up to  $RA \simeq 190^\circ$ . They report two cases of M giants excess along the *los* in common with the present analysis. The most evident at a distance  $D \sim 45$  kpc, compatible with our estimates, and the other one, less pronounced, at a distance  $D \sim 20 - 25$  kpc, for which the interpretation is not so clear as in the case of A stars and RR Lyrae detections.

All the detections mentioned above, as well as others

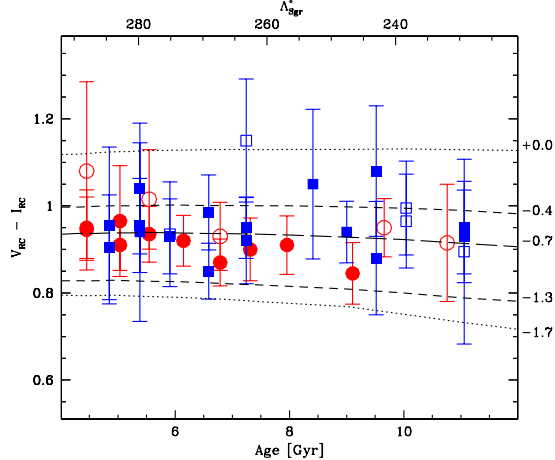


FIG. 18.— De-reddened color of the observed RC peaks as a function of  $\Lambda_{Sgr}$ . The observed points are compared with the predictions of the Girardi & Salaris (2001) theoretical models for different metallicities, plotted as a function of age of the population in the range 4–12 Gyr. The scale on the lower horizontal axis (age) refers to models, that on the upper horizontal axis ( $\Lambda_{Sgr}$ ) refers to observed points.

toward specific directions, also not included in the range considered here (Martínez-Delgado et al. 2001, 2004; Belazzini et al. 2003b; Vivas & Zinn 2006), are collected and reported in Fig. 17 of M03. This figure, as well as Fig. 19 in Law & Majewski (2010), clearly illustrates how it may be difficult and misleading to put results from different sources (and on different distance scales) all together. In this sense, it is more fruitful to compare our results with other data sets providing homogeneous distance estimates for significant portions of some wrap in common with those detected here.

For instance, Bel06, who used A-F dwarf stars from the SDSS to trace the Stream, detected a distant gradient along the main wrap of the leading arm that is in good agreement with our results (for both branches). More interestingly, Bel06 found a double detection in a few branch A *los* (from F5A to F7A): in addition to the main wrap of the leading arm, they found also a more distant structure,  $\sim 15$  kpc behind. This finding is also in excellent agreement with our results (see Sect. 4.1). The only difference is that we detect this structure, at similar distance, also in the corresponding branch B fields.

Newberg et al. (2007) investigated the relationship between several previously-identified substructures in the direction of Virgo and the Sgr Stream using imaging and spectroscopic observations of F stars and BHB stars from SDSS and SEGUE. In their Tab. 1, they reported the detections associated to the Sgr Stream, providing also estimates of the distance of these structures. This allowed us to perform the direct comparison with our results that is presented in Fig. 19. The agreement for the structure detected in both studies (main wrap of the leading arm) is very good, both for branch A and B.

Niederste-Ostholt et al. (2010) investigated the leading arm of Sgr Stream in the same region of the “field of stream” analyzed by Bel06, using BHB candidates from the SDSS. The distances to BHBs are calculated assuming an absolute magnitude  $M_g = 0.7$  and are in good agreement with the results of Bel06. In Fig. 19 we compare our estimates with those obtained by Niederste-Ostholt et al. (2010), reported in their Tab. 1, in the

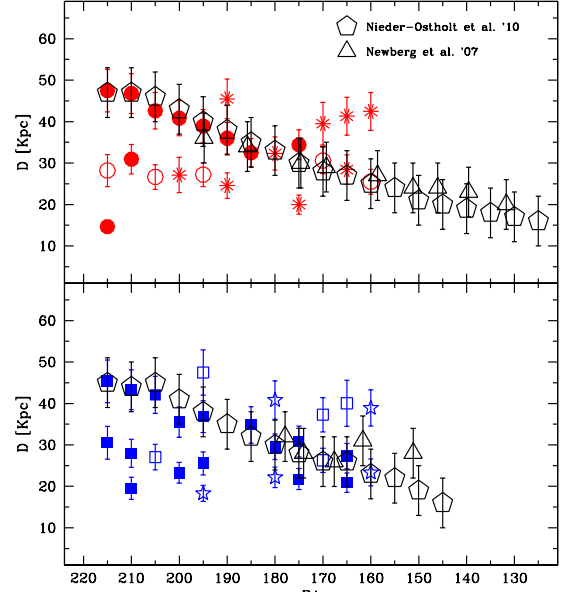


FIG. 19.— Comparison between our distance estimates (same symbols as in Fig. 13) and those by Newberg et al. (2007, open triangles) and by Niederste-Ostholt et al. (2010, open diamonds). The match between the different indicators is remarkably good, for the portions of the leading arm considered by the three studies. The trailing arm is detected only in the present study.

region of sky going from  $RA \geq 160^\circ$  to  $RA \leq 220^\circ$ . Our distances are calculated using a true distance modulus of  $(m - M)_0 = 17.10$ , roughly the same adopted by Niederste-Ostholt et al. (2010) (the  $g$  magnitude of the BHB in the main body is  $g \sim 17.80$ ). In all the regions where the data-sets overlap the match is very good, both for branch A and B detections. The trailing arm of Sgr Stream is not sampled by Niederste-Ostholt et al. (2010) that concentrated their analysis on the detection of the leading arm and on an accurate distance estimate for this wrap of the Stream.

In conclusion, the overall agreement with previous detections of the leading arm is very good. The situation for the other coherent structures detected here is more difficult to judge; in our view the only firm conclusion that can be drawn is that several independent studies found evidence for some structures located in front of the main wrap of the leading arm, in the considered range of  $\Lambda$ . It is unclear if some of these detections can be associated with the constant distant (putative) wrap of the trailing arm detected here or to even more nearby wraps. In this sense it is interesting to note that a similar coherent structure, at a similar distance, is detected also by Keller (2009b), using SGB stars (see his Fig. 7).

## 6. COMPARISON WITH MODELS

As soon as it was realized that Sgr was likely undergoing tidal disruption, several authors attempted to model the process by means of N-body simulations, to establish the plausibility of proposed models and to infer the properties (mass, orbit) of the original system (Velazquez & White 1995; Johnston et al. 1995; Ibata et al. 1997; Edelsohn & Elmegreen 1997; Ibata & Lewis 1998; Gómez-Flechoso et al. 1999; Johnston et al. 1999; Jiang & Binney 2000; Helmi & White 2001). It is interesting to note that Velazquez & White (1995) were able to provide estimates of perigalactic and apogalactic distances and or-

bial period remarkably similar to those obtained in the most recent studies, just one year after the discovery of Sgr ( $R_{peri} \simeq 10$  kpc,  $R_{apo} \simeq 52$  kpc and  $P_{orb} \simeq 0.76$  Gyr, to compare, for instance, with  $R_{peri} \simeq 15$  kpc,  $R_{apo} \simeq 60$  kpc and  $P_{orb} \simeq 0.85$  Gyr, from Law et al. 2005). The possible rôle of Sgr in the formation of the Galactic Disk warp was studied by Ibata & Razoumov (1998) and Bailin (2003).

However, since the Sgr Stream appears as a remarkably-coherent structure crossing a large part of the Galactic halo on a nearly-polar orbit, it seems the ideal tracer to study the overall shape and the degree of clumping of the Galactic halo as a whole. For this reason, the most recent N-body modeling efforts have focused on constraining the shape of the DM halo of the Milky Way (Ibata et al. 2001b; Martínez-Delgado et al. 2004; Helmi 2004; Law et al. 2005; Johnston et al. 2005; Fellhauer et al. 2006; Law et al. 2009; Law & Majewski 2010). However it turned out that the conclusions of these studies depended on the specific set of observational constraints considered, and it is now generally accepted the idea that none of the static-potential axisymmetric halo models considered is able to reproduce simultaneously all the available positional and kinematic data (see Yanny et al. 2009a; Law et al. 2009, for references and discussion). In a recent contribution Law et al. (2009) anticipated that the adoption of triaxial halo models can help to solve this problem: in Sect. 6.3 we briefly consider the N-body model they produced as a follow-up of that analysis (Law & Majewski 2010). In any case, it is quite clear that currently available models are far from perfect, and more detailed simulations are needed to extract all the possible information on the Galactic DM halo from the Sgr Stream, as more (and more accurate) observational constraints become available. For example, Fellhauer et al. (2006) interpreted the bifurcation of the trailing arm giving rise to the A and B branches considered here as produced by the precession between two subsequent orbits. As the implied amount of precession is relatively small, this, in turn, requires that the potential felt by Sgr should be nearly spherical. However the similarity between the two branches (in terms of distance, kinematics and stellar content) led Yanny et al. (2009a) to suggest that in fact the two branches are composed by stars lost at the same epoch, i.e. they are in the same orbital phase. In this case the separation between the two branches would not be related to orbital precession and would have nothing to say about the shape of the potential. In their recent analysis, Niederste-Ostholt et al. (2010) adopt the same view as Yanny et al. (2009a)<sup>16</sup>.

In the present contribution we provide very accurate distance estimates along the northern branches of the Sgr Stream as powerful constraints for future generations of Sgr disruption models that will include effects like halo triaxiality, dynamical friction, time-evolving Galactic potential, etc. In this section we discuss our findings in comparison with the predictions of the three models by Law et al. (2005, L05 hereafter), just to show how powerful accurate distance constraints can be in distinguishing between different models (some examples of such comparisons have already been presented in Sect. 3.2 and Fig. 13). One of the main aims of the studies by L05

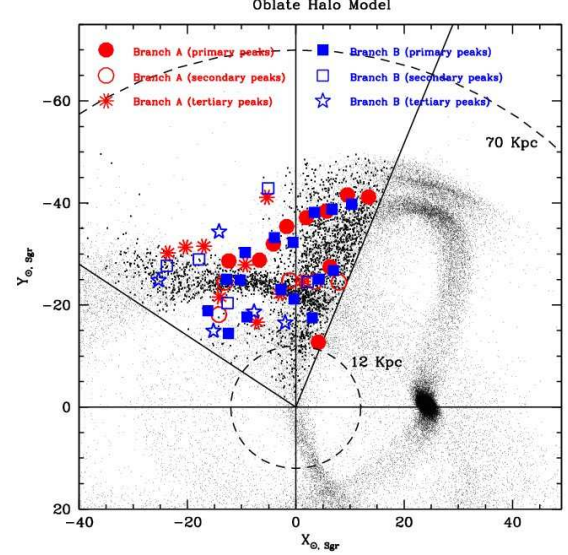


FIG. 20.— Comparison between the positions of the observed RC peaks and the predictions of Law et al.'s N-body model of the disruption of Sgr within an *oblate* DM halo in the  $X_{\odot, Sgr}$  vs.  $Y_{\odot, Sgr}$  plane (i.e. the approximate plane of Sgr orbit seen face-on). Heavier dots indicate model particles enclosed in our FoVs cones. To be consistent with Law et al. (2005) we converted our differential distances into absolute ones by assuming a true distance modulus of 16.90 for the main body of Sgr.

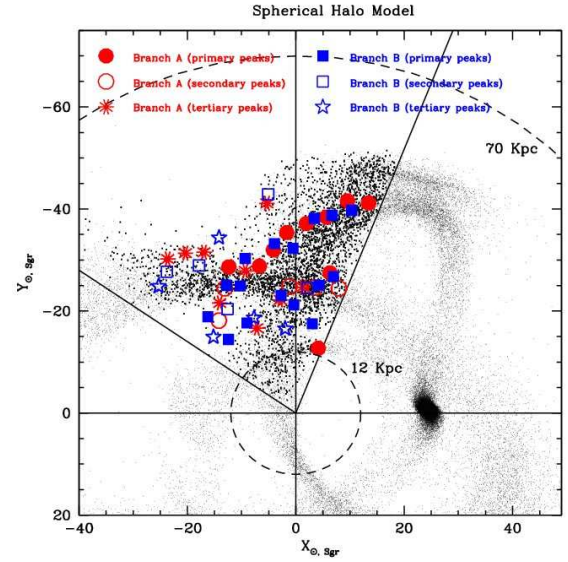


FIG. 21.— The same as Fig. 20, but for a N-body model within a *spherical* DM halo.

and Johnston et al. (2005), was to use the existing observations on the Sgr Stream to constrain the shape of the Galactic halo. For this reason the three models they provide<sup>17</sup> describe the final state of the evolution of a realistic progenitor of Sgr after a few orbits within a Galactic potential having a *prolate*, *spherical*, or *oblate* DM halo. For sake of simplicity, in the following we will refer to these models as to the Oblate (O), Spherical (S) and Prolate (P) models, respectively. In all the models, each particle is flagged according to the peri-galactic passage in which it became unbound from the main body of the galaxy. Here we refer to stars still bound or lost

<sup>16</sup> See also the discussion in Law & Majewski (2010).

<sup>17</sup> Publicly available at <http://www.astro.virginia.edu/srm4n/Sgr>

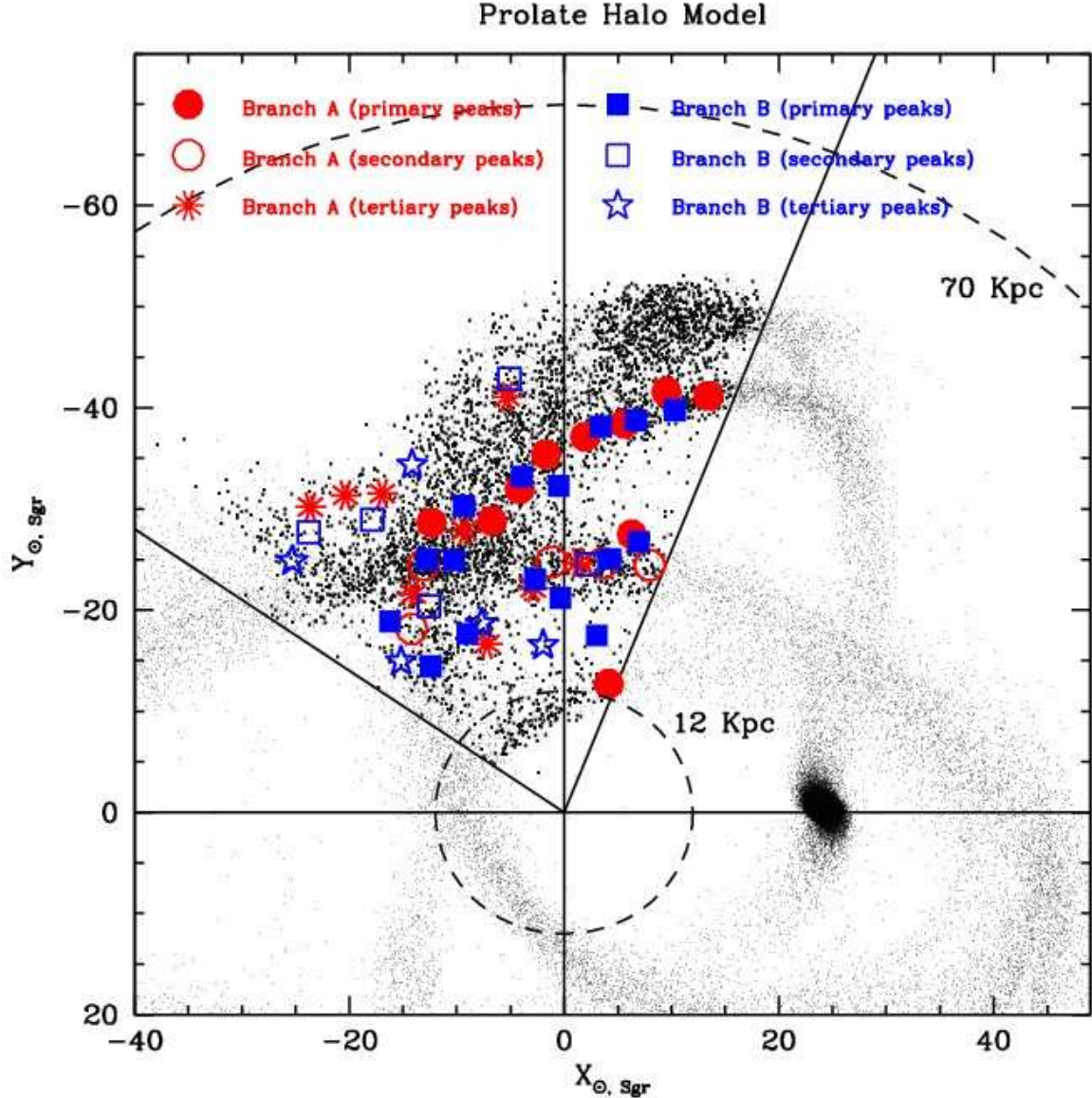


FIG. 22.— The same as Fig. 20 and 21, but for a N-body model within a *prolate* DM halo.

during the current peri-galactic passage as having  $p = 0$ ;  $p = -1, -2, -3, -4$  refers to particles lost one, two, three and four peri-galactic passages ago, respectively.  $p = 0$  stars are out of the range accessible with the fields considered here, according to the L05 models. When we speak of “young” and “old” wraps of the Stream we refer to portions of the Stream whose population is dominated by particles lost in the most recent or less recent peri-galactic passages, respectively, on an age-scale encompassing the last  $\sim 5$  orbits, i.e.  $\sim 3 - 4$  Gyr.

In Figg. 20, 21 and 22 the three models are compared with the positions of the observed RC peaks in the  $X_{\odot,Sgr}$  vs.  $Y_{\odot,Sgr}$  plane<sup>18</sup>, as in Fig. 11, above. It is immediately apparent from Fig. 20 that the trend traced by our primary peaks rules out the O model, that fails to reproduce the most prominent branch of the Stream

seen in SDSS data, i.e. the portion of the leading arm descending from the North Galactic Pole (while there is some agreement for the - putative - nearby portion of the trailing arm). The case of the spherical model is similar, even if the disagreement between observations and model prediction is less severe (Fig. 21).

The comparison with the prolate model is the most interesting and we take it also as the occasion to describe the trends found in our data in a deeper detail. For a more fruitful discussion we provide Fig. 22 in a larger format with respect to its analogs for the oblate and spherical models (see also Fig. 13). It should be stressed that, in the following, we interpret the coherent structures we have detected using this specific model as a guideline. For an example of a different interpretation see Sect. 6.3, below. There are several features worth noticing in Fig. 22:

1. For  $X_{\odot,Sgr} \gtrsim -7$  kpc the agreement between the positions of our primary branch-A peaks and the portion of the leading arm going from  $(X, Y) \simeq$

<sup>18</sup> For brevity, in the following we will drop the  $\odot, Sgr$  index any time we found this convenient;  $X_{\odot,Sgr}$ ,  $Y_{\odot,Sgr}$  and  $X$ ,  $Y$  are interchangeable. For the same reason, the values of  $X$ ,  $Y$  must be always intended as expressed in kpc, even if not explicitly stated.

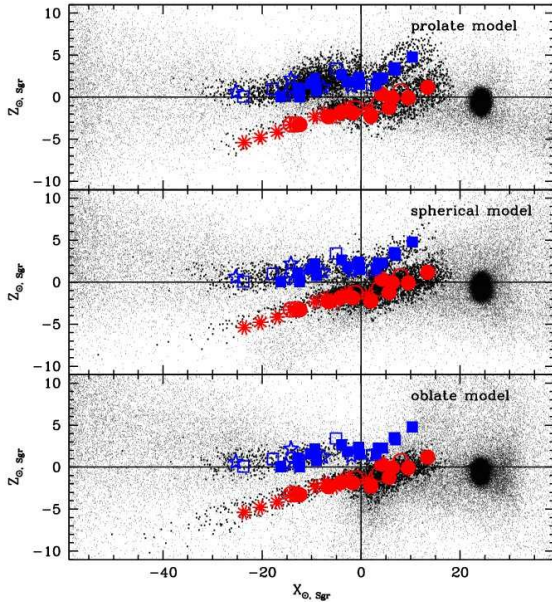


FIG. 23.— Comparison of observed peaks positions with Law et al.’s models in the  $X_{\odot,Sgr}$  vs.  $Z_{\odot,Sgr}$  plane (i.e. perpendicular to the orbital plane of Sgr, that is seen edge-on). The symbols are the same as in Fig. 20.

$(16, -40)^{19}$  to  $(X, Y) \simeq (-7, -28)$  is *excellent*. Also primary branch-B peaks follow the same trend thus confirming that the two structures lie at *the same distance* (see also Fig. 13, and Belokurov et al. 2006; Fellhauer et al. 2006; Yanny et al. 2009a). According to the considered model, this part of the leading arm is dominated by  $p = -1$  particles up to  $X_{\odot,Sgr} \simeq 0$ , and by a mix of  $p = -2$  and  $p = -3$  particles for  $X_{\odot,Sgr} \lesssim 0$ .

2. Several detections seem to extend the path of the arm down to  $(X, Y) = (-15, -15)$ , possibly suggesting a slightly less elongated shape of the arm with respect to the model predictions. The coherence of the structure is less clear in this region: the models predict that various wraps cross here and this may be source of some confusion.
3. The model predicts the presence of a more ancient (mostly populated by  $p = -2$  and  $p = -3$  particles) and wider wrap running nearly parallel to the portion of the leading arm described above, but behind it. This structure has been detected in branch-B, where one flag=2 point, at  $(X, Y) \sim (-5, -44)$ , in coincidence with a branch-A detection, and a flag=3 detection at  $(X, Y) \sim (-14, -35)$ . These points appear to trace the outer edge of this wrap, as depicted by the considered model. On the other hand, there is no detection (in any branch) for  $X \gtrsim 0$ , i.e. where the detection of the second wrap should be easier, according to the model, as the separation from the inner wrap increases with  $X$  and the feature is denser and narrower in that region. This lack of detection seems confirmed by the independent results of Belokurov et al. (2006), that, however, detect the most distant wrap at  $X < 0$  only in the direction of Branch A. To have a deeper

<sup>19</sup> In the following we drop the  $\odot, Sgr$  indices, for brevity. The unity is always kpc.

insight into this problem in Fig. 24 we provide a direct comparison between observations and model at the SCP level, as done in Fig. 12. Here we compare the observed SCP of the F1A, F2A and F3A fields with the SCPs obtained from the model in the considered *los* for particles lost one, two, three and four peri-galactics ago. From the upper-right panel it is clear that the dense  $X > 0$  part of the outer wrap, produced by  $p = -2$  particles in the model, has no counterpart in the observed SCPs and would be easily detected if actually there. On the other hand, the sum of the relics having  $p = -1, -3$ , and  $p = -4$  provide a satisfactory match to all the observed peaks. This suggests that there is a real mismatch between the L05 P model predictions and our observations in this part of the halo. We note that the spherical model suffers from the same problem, while the oblate model does not predict a strong signal at that position, but it fails to match all the observations at  $X < 0$  for this wrap.

4. A coherent series of detections lying at nearly constant  $Y \sim 25$  kpc, traced from  $X \sim 8$  to  $X \sim -14$  in both branches, traces a filamentary structure that is identified here for the first time. Isolated detections with M giants and RR Lyrae were previously reported at  $\Lambda \simeq 295^\circ$  (Majewski et al. 2003; Vivas & Zinn 2006; Ivezić et al. 2000a). This feature matches quite well a wrap of the trailing arm that is present in all the L05 models; it can be appreciated from Fig. 13 and Fig. 22 that the agreement with the P model is very good. For  $X < -14$  however the positions of the peaks do not trace the model prediction anymore. This apparent discontinuity along this branch cannot be (only) due to the distance effects discussed in Sect. 2.3 as the distance is expected to increase and the sensitivity of the method should increase accordingly. Moreover we are able to detect peaks both more and less distant than the position predicted by the model along these *los*. This feature has no counterpart in the triaxial halo model discussed in Sect. 6.3, below. It is clear that additional information is needed to understand better the nature of this structure, from, for example, the kinematics of member stars.
5. There are primary and tertiary branch-B detections, plus one tertiary branch-A detections, tracing a feeble (but coherent) spur from an ancient ( $p = -3, -4$ ) wrap, predicted by the model to arch between  $(X, Y) \sim (-10, -15)$  and  $(X, Y) \sim (-3, -22)$ . As far as we know this is the first detection of this nearby portion of the Stream. A couple of primary branch-B detections (and a tertiary branch-A detection) may trace similar substructures on the near side of the constant-distance portion of the trailing arm (see Sect. 6.3 for an alternative interpretation).
6. There are a couple of other cases of slight distance mismatches between branch-A and branch-B detections, occurring, however in the region around  $(X, Y) \sim (-10, -25)$  where different wraps of the Stream cross each other. It may be challenging to disentangle the various contributions based

on distances alone. A more interesting case is provided by the two pairs of detections around  $(X, Y) \sim (-23, -30)$ , a region where the model predicts only feeble structures and branch-B detections are clearly more nearby than branch-A ones. It is intriguing to note that the few particles of the model lying in this region are not uniformly distributed but appear to form two approximately parallel tiny bridges that reasonably reproduce the observed pattern. Also in this case this is the first detection of such structures.

7. Both the P and S models by L05 predict the presence of a fairly dense and narrow wrap composed by  $p = -3$  and  $p = -4$  particles crossing the accessible range of the X, Y plane from  $(X, Y) \sim (-7, -7)$  to  $(X, Y) \sim (5, -12)$ , where it emerges from the  $d \lesssim 12$  kpc zone of insensitivity of our method (the triaxial model briefly discussed in Sect. 6.3 also displays a similar feature). Here we have a primary detection from the SCP of F1A, that currently is the first detection of this nearby wrap of the leading arm<sup>20</sup>. A detailed exploration of the  $d \lesssim 12$  kpc zone would require a different kind of analysis, hence it is postponed to a future contribution. We note, however, that Monaco et al. (2007) studied the chemical composition and the kinematics of a small sample of M giants that can be attributed to this nearby wrap.
8. Two Branch-B detections, located at  $(X, Y) \sim (-3, -16)$  and  $(X, Y) \sim (+3, -18)$ , F5B and F2B, respectively, do not seem to match any significant structure of the spherical and prolate L05 models; the primary one (that with positive X) is marginally consistent with the part of the leading arm plunging toward the Sun of the oblate model (but see Sect. 6.3, below). As anticipated in Sect. 4.1, their position [(RA, Dec) =  $(195^\circ, +16^\circ)$   $d \sim 18$  kpc, and (RA, Dec) =  $(190^\circ, +18.5^\circ)$   $d \sim 19.5$  kpc, respectively] is fully compatible with the outer fringes (i.e., the high Galactic latitude edge) of the nearby overdensity S297+63-20.5, discovered by Newberg et al. (2002) and discussed in detail in Newberg et al. (2007). It is unclear why we do not detect the structure in other adjacent fields, or in the corresponding branch A fields. This may be due to the intrinsic weakness of the RC signal from these nearby features, or it may reflect a high degree of complexity of the sub-structures, as suggested in the analyses by Keller et al. (2009) and Vivas et al. (2008). Newberg et al. (2007) provided positional and kinematic evidence arguing against the association of S297+63-20.5 with the Sgr Stream, that was originally proposed by Martínez-Delgado et al. (2007) and cannot be completely ruled out at the present stage (see also the discussion in Law & Majewski 2010). However

<sup>20</sup> While the distinction between *leading* and *trailing* arms is easy and sensible for particles lost in the latest two peri-galactic passages, it becomes increasingly blurred for Stream wraps dominated by more ancient relics, as a particle can reach the same position in these parts of the Stream both from the leading and from the trailing sides of the tidal tails.

Fig. 22 provides further support for the conclusions by Newberg et al. (2007): the peaks detected here do not present any continuity with the main branches of the leading and trailing arms of the Stream as traced in the present analysis (but see also Sect. 6.3, below). Our data suggest that the leading arm crosses the Galactic plane at  $\sim 10$  kpc from the Sun, toward the Anticenter, in agreement with Newberg et al. (2007) and Seabroke et al. (2008). On the other hand, the identification of S297+63-20.5 with the Virgo Stellar Stream (VSS, Duffau et al. 2006; Vivas et al. 2008) seems likely, while the relationship between VSS and the Virgo Over Density (VOD, Jurić et al. 2008; Newberg et al. 2007; Keller et al. 2009) is less certain (see Newberg et al. 2007; Keller 2009b). We are currently following up these possible detections of S297+63-20.5/VSS in F5B and F6B (also looking for the structure at lower latitudes). If confirmed, they would provide the first detection of RC stars in these structures, in analogy with the cases of Boo III discussed in Correnti et al. (2009). RC stars may provide new insights on the nature of complex series of structures recently identified in the direction of Virgo (Keller et al. 2009; Keller 2009b).

All the features and correlations with the P model described above can be seen even more clearly and directly in Fig. 13, that provides the most natural way to compare our measures with models. For example, the match between two weak model structures described at point 6, above, and our detections can be very clearly appreciated in that plot, at  $230^\circ \lesssim \Lambda \lesssim 245^\circ$  and  $d \simeq 37$  kpc. The linear trend of increasing distance with decreasing  $\Lambda$  of the two parallel sets of observed points is very nicely matched by corresponding filaments of particles in the model.

Fig. 23 shows that the overall morphology of the three models is remarkably similar in the  $X_{\odot, Sgr}$  vs  $Z_{\odot, Sgr}$  plane and reproduces the general trends of the data (except for the Oblate model, that predicts a total lack of particles for branch-B detections at  $X_{\odot, Sgr} > 0$ , at odds with observations). A more detailed analysis is beyond the scope of the present paper. On the other hand, we must conclude, from the results summarized above, that the *prolate* model by Law et al. (2005) is the one (among those considered here) providing the best match to the positional data considered here. It should be stressed that with this *we do not intend to say that a prolate halo model is favored by our data*, as the comparison was limited to just three very specific models that are already known not to be able to fit all the positional and kinematical observational constraints available (Law et al. 2009). In particular it should be recalled that the available radial velocities of Stream stars seems to favor prolate models (Helmi 2004), while the angular precession of the leading arm with respect to the trailing arm favor spherical or slightly oblate models (L05; Johnston et al. 2005; Newberg et al. 2007; Prior et al. 2009a, and references therein). We simply note that any future model intended to fit all the observed characteristics of the Sgr Stream must have a spatial structure *very similar* to that of the *prolate* model by Law et al. (2005), at least in the

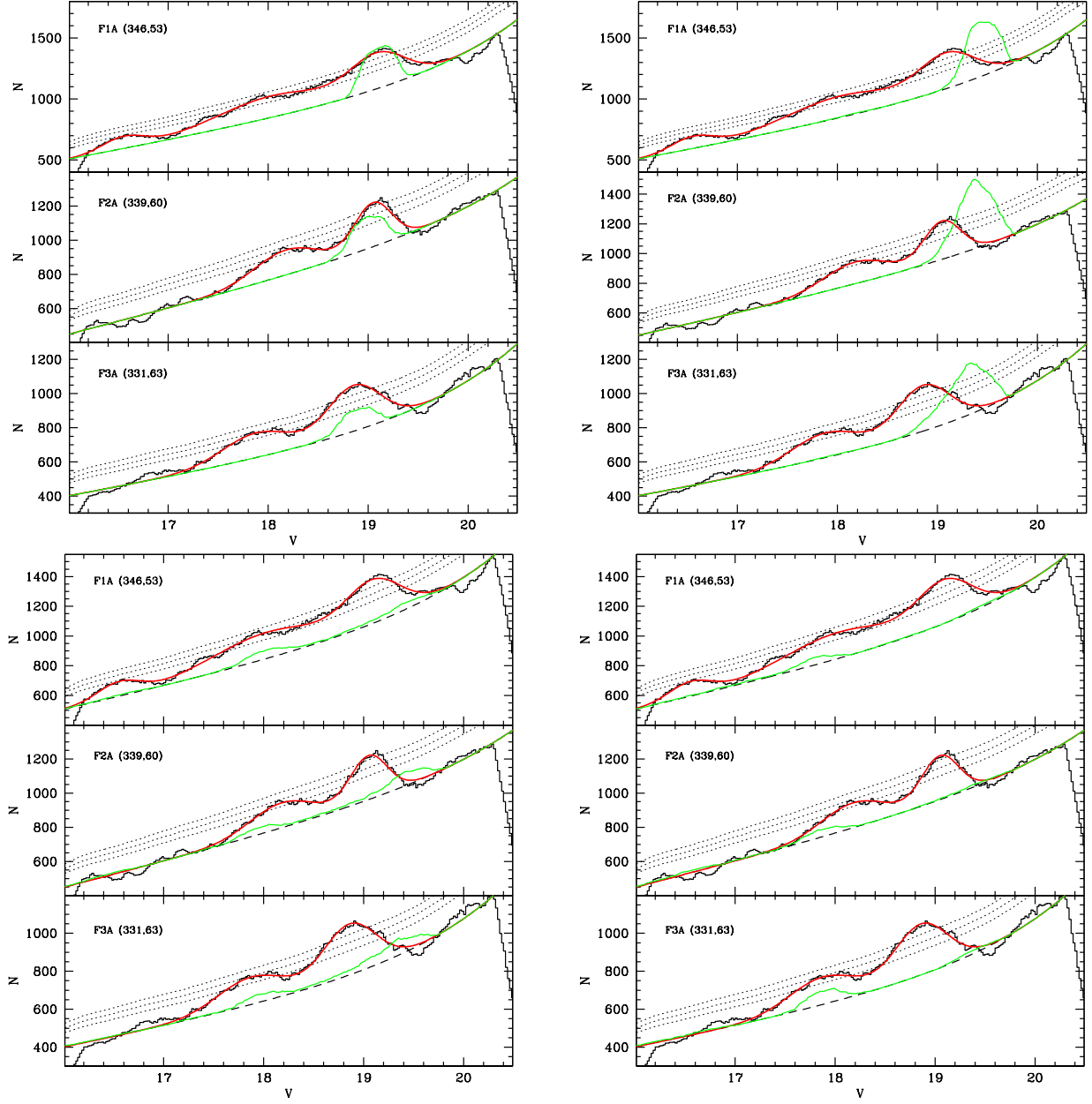


FIG. 24.— Comparison of the observed SCPs in the field F1A, F2A, F3A with the synthetic SCPs obtained by adding the (arbitrarily normalized) *los* histogram from the prolate N-body model (as in Fig. 12 above) to the best-fit background model of the considered field. Each of the four (triple) panels report the synthetic SCPs including only N-Body debris stripped from the main body one, two, three or four orbits ago, going from the upper left, to the upper right, to the lower left and to the lower right panels, respectively.

portion of space sampled by our study, unless an alternative origin is assumed for the  $d \sim 25$  kpc structure we tentatively interpreted as the trailing arm.

#### 6.1. Trends of depth as a function of orbital azimuth

In line with the above discussion, in Fig. 25 we compare the FWHM along the *los* described in Sect. 3.5 with those measured from the distribution of particles of the Prolate model of L05, along the same *los*. The following discussion is mainly intended to illustrate the possible use of the derived FWHM. It should be considered that there are additional sources of uncertainty affecting this comparison, associated with the the measure of FWHM in models. For example, the measured width depend on the actual number of particles of the model, the limited number of particle may lead to underestimates of the

actual width. This expected effect is clearly confirmed in Fig. 25, where observed FWHM are always equal or larger than their model counterparts. The disentanglement of overlapping structure may be also problematic, as it is unavoidably performed in different ways in the observed SCPs and in the N-body models.

To minimize the possible ambiguities associated with the collapse of complex structures along the *los* into a single FWHM measure (see Sect. 3), especially in regions where different wraps cross one another, in Fig. 25 we limit our comparison to  $X > -10$  kpc peaks tracing the two main wraps (leading and trailing arms) that are 30 kpc apart at  $\Lambda_{Sgr} = 290^\circ$  and cross each other at  $\Lambda_{Sgr} = 265^\circ$ , and we consider only primary and secondary peaks.

The most interesting and sensible comparison is between the trends of the FWHM as a function of orbital

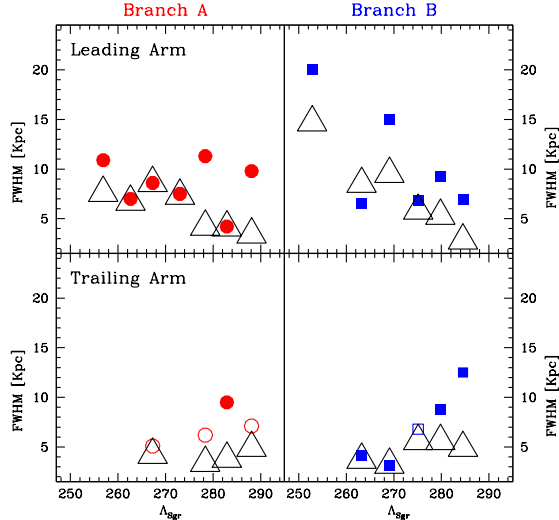


FIG. 25.— Comparison between the trends with  $\Lambda_{Sgr}$  of the observed FWHM along the *los* (the same symbols as Figs. 20, 21 and 22, above, and the predictions of the Prolate model by L05 (open triangles). The comparison is limited to the *los* from F1 to F7 (i.e., those providing the cleanest tracing of the leading and trailing arms). The upper row of panels refers to detections in the leading arm, the lower row to detections in the trailing arm. The left and right columns refer to branch A and branch B, respectively. The field numbers increase (from F1 to F7) from right to left, as in Fig. 13 and Figs. 20, 21, 22.

azimuth. The upper panels of Fig. 25 show that the observed and predicted trends for the leading arm are indeed similar, both in direction and in amplitude, for both branches. The agreement of the absolute values of the FWHM is also satisfying (within a factor of  $\sim 2$ ), with four Branch A and one Branch B detections closely matching the model predictions. The FWHM of the considered detections from F1A and F3A give some reason of concern, as they break the continuity of the observed trend: this may suggest that there may be some unresolved structure in these peaks. Alternatively we have to accept variations of a factor of  $\sim 2$  as due to the uncertainty inherent to the adopted method of estimating FWHM. The overall agreement is reasonable also for the putative trailing arm.

It is interesting to note that the different trends observed in the two branches of the leading arm are reproduced by the P model that do not present any bifurcation (see also Fig. 26, for a similar behavior in the  $\Lambda$  vs. density trend in the leading arm).

## 6.2. Trends of density as a function of orbital azimuth

In strict analogy with the analysis described in the previous subsection, in Fig. 26 we present the comparison of the observed and predicted trends of the stellar density (see Sect. 3.4) as a function of  $\Lambda$ . The measured density is compared with the density of particles in the same wrap of the P model. The density scale of the model has been multiplied by the arbitrary factor 2.5, to achieve a reasonable normalization with the observed values. As in Sect. 6.1 the comparison presented is just intended as illustrative of the possible use of these numbers, and it is limited to the cleanest portions of the leading and trailing arms, at  $X > -10$  kpc.

For the leading arm the match between the overall observations and the models is acceptable, in particular for branch A. The highly discrepant point at  $\Lambda \sim 263^\circ$  is

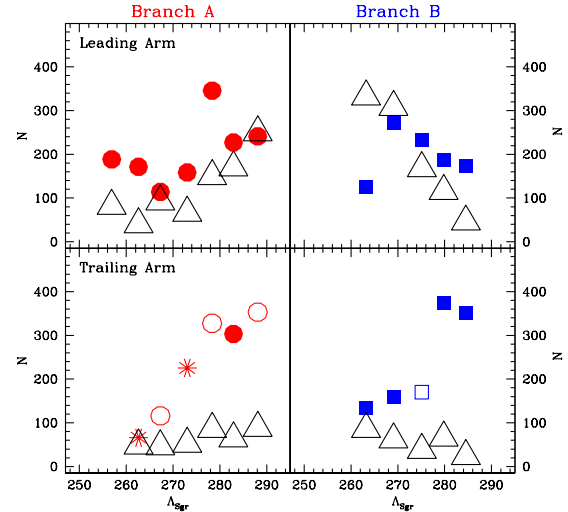


FIG. 26.— The same as Fig. 25 for the density of RC stars as a function of  $\Lambda$ . An arbitrary normalization factor of 2 is applied to all the density values from the theoretical model.

associated with an especially complex SCP model, with three overlapping peaks (F5B): for this reason we are inclined to ascribe the discrepancy to an erroneous density estimate.

On the other hand, while the model predicts low or even negative gradients of density with increasing  $\Lambda$ , the observations show a very strong positive gradient, similar in both branches<sup>21</sup>. This is an obvious example of the kind of constraints that can be achieved with these data: in principle, any fully successful model of the disruption of Sgr must also reproduce a density gradient similar to the observed one. However it has to be taken into account that the available models are intended to describe the dark matter halo in which the baryonic part of the galaxy is embedded. While, for example, stars and DM particles in the Stream should not greatly differ in their kinematical and positional properties, their density would follow the same trends only if mass strictly follows light also in tidal tails, which is very unlikely to be the case (see Peñarrubia et al. 2008, and references therein).

## 6.3. The triaxial model by Law & Majewski 2010

When the present manuscript was ready for submission, a preprint was posted (Law & Majewski 2010), following up the preliminary analysis by Law et al. (2009). In that study a new N-body model of the disruption of Sgr within a triaxial Galactic potential, is shown to provide a reasonable match to most of the existing observational constraints. In particular, the new model reproduces the distance *vs.*  $\Lambda$  trend reported by Bel06 for the main wrap of the leading arm, the precession between the leading and trailing arms, and it matches the existing sets of kinematic measures.

As we have stressed before, it is far beyond the scope of the present analysis to find out which is the best available model. However it is worth showing the comparison between our results and this new model, for complete-

<sup>21</sup> It has to be recalled that the bifurcation in two branches is an observed property of the main wrap of the leading arm. There is no reason to discuss other wraps as divided into two branches: here this is merely incidental, due to adopted distribution of the observed fields that were chosen to trace the bifurcation.

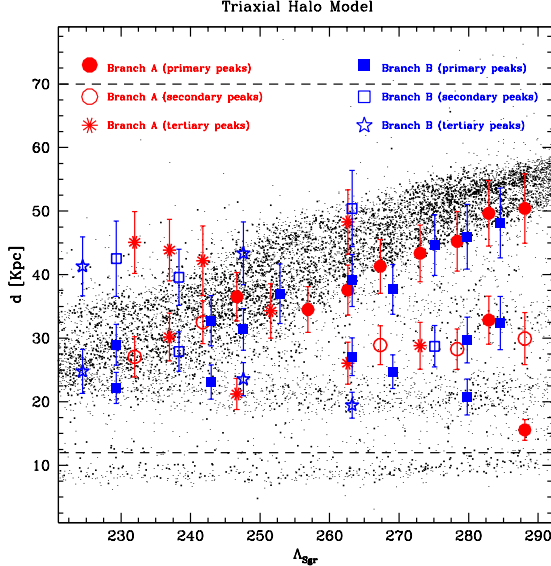


FIG. 27.— Comparison with the new “triaxial halo” (T) model by Law & Majewski (2010): distance vs. orbital azimuth. Symbols are the same as in Figg. 20, 21 and 22. Our measures have been rescaled to match the distance scale adopted by Law & Majewski (2010), that implies a distance to the main body of Sgr  $d = 28$  kpc (i.e.  $(m - M)_0 = 17.23$ , instead of  $(m - M)_0 = 16.90$ , as adopted by L05).

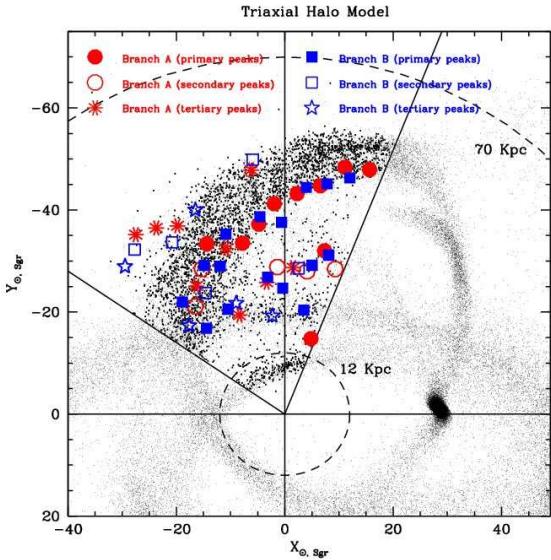


FIG. 28.— Comparison with the new “triaxial halo” (T) model by Law & Majewski (2010): the  $X_{\odot,Sgr}$  vs.  $Y_{\odot,Sgr}$  plane, with the same assumptions and symbols as Fig. 6.3.

ness and (above all) as a very instructive example of how the interpretation of observed features may depend on the considered model (see Sect. 7 for discussion). From the inspection of Fig. 27 and Fig. 28 it can be concluded that the triaxial halo model provides a reasonable match to distance gradient of the main wrap of the leading arm, over the whole range of  $\Lambda$  covered by our data. This is not unexpected as the model is found to fit the observations by Bel06 in this regard, and we are in good agreement with these authors. The same is true for the sparse detections behind the main wrap, that were also found by Bel06. It is interesting to note that, in a similar fashion to the P and S models, the T model predicts a remark-

able increase of the density of this wrap for  $\Lambda \gtrsim 275^\circ$  ( $X \gtrsim 0$ ) that is not observed, neither in the present work or by Bel06. Moreover, the T model does not seem to display the narrow and dense structure of the main wrap of the leading arm that in the P model appears to match so well our coherent set of primary detections in that region. We postpone a detailed comparison between the observed structure along the *los* and the predictions of the P and T model to a future contribution: here we limit the discussion to the main features of the models (i.e. trends of distance with orbital azimuth).

The new model makes predictions very similar to those of the P and O models also regarding the nearest wrap of the Stream, running across the whole range of  $\Lambda$  sampled by our data. However it should be noted that it predicts this wrap to lie below our sensitivity limit at any  $\Lambda$ , in the observed range, thus it is unable to match the observed points at  $\Lambda \simeq 287^\circ$  and  $d \simeq 13$  kpc, at odds with the P model. The T model presents a very coherent narrow wrap of the trailing arm running at nearly constant  $d \simeq 20$  kpc from  $\Lambda \simeq 290^\circ$  to  $\Lambda \simeq 250^\circ$ , then it begins to bend gently toward  $d \simeq 25$  kpc from  $\Lambda \simeq 235^\circ$  where it crosses with the leading arm. This feature matches *very nicely* the nearby ( $d \leq 25$  kpc) detections that we tentatively attributed to S297+63-20.5/VSS and to an ancient spur of the leading arm, in the comparison with the P model described in detail in Sect. 6, above.

On the other hand, the coherent structure we detect from  $\Lambda \simeq 260^\circ$  to  $\Lambda \simeq 250^\circ$ , that we interpreted as a wrap of the trailing arm, is not present in the T model. The same is true for the  $d \geq 40$  kpc structures at  $\Lambda \leq 245^\circ$ . The orbital path of the simulated Sgr galaxy matches also these structures, so it is not excluded that they may correspond to very ancient wraps. However, it has to be noted that the T model is the remnant of the evolution of a Sgr progenitor for  $\simeq 8$  orbits (not just  $\sim 4$  as for S, O, and P) models, thus it should include wraps populated from more ancient stripping events than the S, O, and P models.

In conclusion, while the P model still appears to provide a more thorough match of the observed structures, the T model provides a promising alternative that deserves to be investigated in further detail. Not surprisingly, the mere comparison with our own (limited) data-set shows that both models need to be refined.

## 7. SUMMARY AND CONCLUSIONS

We have used RC stars to trace the long tidal tail of the Sgr dSph galaxy in the portion of the Northern sky sampled by the SDSS-DR6. Structures along the line-of-sight are identified as peaks in the (otherwise smoothly increasing)  $I$ - and  $V$ -band SCPs of color-selected samples of candidate RC stars, from  $\sim 5^\circ \times 5^\circ$  fields covering the whole extension of the two main branches (A and B) of the Sgr Stream identified by Belokurov et al. (2006) in the same dataset. Any other part of the Stream in addition to these branches is expected to lie (approximately) in the same plane, i.e. it should be visible in the considered fields. The analysis was focused on obtaining the most accurate and reliable distances to all the wraps of the Stream that we were able to detect.

Many significant peaks were consistently found in both the SCPs of several fields. The observed SCPs were modeled as a series of Gauss curves (one for each peak)

superposed to a polynomial accounting for the smooth fore/background population. For each significant peak we derived a purely differential estimate of its distance (with uncertainties  $\leq 10\%$ ), an estimate of the FWHM along the *los*, and an estimate of the associated density of RC stars attributable to the considered structure. All the derived quantities are provided in Tab. 2 as powerful constraints for the new generations of models of the disruption of the progenitor of Sgr dSph within the Milky Way halo.

To illustrate the potential of our measures in that context we compared them with the three models made publicly available by L05. These provide a realistic realization of the present epoch configuration of particles that were originally bound to a progenitor similar to Sgr that was evolved for  $\simeq 4$  orbital periods within a static Galactic potential with different degrees of flattening (a spherical, oblate and prolate halo, respectively). The models (and in particular the Prolate halo one, that matches well most of our observations) are also used as guidelines for the interpretation of our results. The great complexity of a structure like the Sgr Stream, multiply-wrapped around the Galaxy, requires a process of convergence between models and observations: the latter must constrain models but the former are indispensable to re-conduce such a complexity to a single structure (see Sect. 6.3).

Our technique resulted in higher-accuracy distance estimates with respect to previous studies, and demonstrated high sensitivity to feeble structures. However, the sensitivity is easily destroyed by contamination from Galactic sources: for these reasons we had to limit our survey to  $b > 50^\circ$ , while other (more abundant) tracers are able to follow the Stream down to  $b > 30^\circ$ . The overall agreement with previous analyses is good (see Sect. 5). Finally, and most importantly, our method proved especially efficient in the detection of (relatively) nearby structures. In the following we summarize and briefly discuss the main conclusions of the present study, taking Fig. 13 and Fig. 22, as references.

- For  $\Lambda \gtrsim 255^\circ$  ( $X \gtrsim -10$  kpc) the leading arm of the Stream is cleanly and coherently detected in both branches, going from  $d = 43$  kpc at  $\Lambda \simeq 290^\circ$  to  $d = 30$  kpc at  $\Lambda \simeq 255^\circ$ . This is in full agreement with the results obtained with other tracers (Newberg et al. 2007; Niederste-Ostholt et al. 2010). This portion of the leading arm is the most unambiguous and robustly constrained.
- In the same range of  $\Lambda$  (and  $X$ ) a remarkably coherent structure is also very clearly detected at nearly constant distance from us,  $d \simeq 25$  kpc. According to the S and P models by L05 this can be interpreted as a wrap of the trailing arm, while it has no obvious counterpart in the recently presented T model (Law & Majewski 2010). The P model matches the observed structure very well. Previous detections of this wrap were reported only around  $\Lambda = 295^\circ$  (see Majewski et al. 2003, for discussion and references).
- The comparison with the L05 models strongly suggest that the run of the relative distance as a function of  $\Lambda$  of the two wraps described above has

a strong power in discriminating between different models of the Stream. In particular the S and O models by L05 clearly fail to reproduce the observed trends. On the other hand the P model reproduces the trend nearly perfectly.

- Weak detections of a further, more distant wrap (running parallel to the leading arm, in the same range of  $\Lambda$  as above) were also obtained. These support similar results by Belokurov et al. (2006). An enhancement of the density of this wrap at  $\Lambda \gtrsim 275^\circ$ , predicted by the S, P and T models, seems to be excluded by the present analysis (in agreement with Bel06).
- Turning to the  $\Lambda \lesssim 255^\circ$  ( $X \lesssim -10$  kpc) portion of the survey, this is characterized by a very complex structure, partly due to the crossing of multiple wraps predicted to occur in this region by all the models. Hence the interpretation of these structures is less straightforward, and must be considered as tentative. However, the P model appears to provide a reasonable match to all the detections in this region: for these reasons we adopt it as a guideline for our best-effort interpretation of the data (see Sect. 6.3 for an alternative view).
- The leading arm seems to be traced beyond  $\Lambda \simeq 255^\circ$ , continuing its trend of linear decrease of its distance down to  $d \simeq 20$  kpc at  $\Lambda \simeq 220^\circ$ . Extrapolating from the observed trend one would expect the arm to cross the Galactic disk at  $\sim 10$  kpc from the Sun, in agreement with the conclusions by Newberg et al. (2007); Seabroke et al. (2008); Law & Majewski (2010). The degree of coherence of the detections in this portion of the leading arm is lower, suggesting the possible presence of further (unresolved) substructure or due to higher uncertainties associated to weaker and overlapped structures.
- In the same region, the continuation of the trailing arm is coherently traced where predicted by the P model up to  $\Lambda \gtrsim 240^\circ$  ( $X \gtrsim -15$  kpc). For  $\Lambda \lesssim 235^\circ$ , in particular, we lack any detection corresponding to the well defined structure predicted by the model (the same is true for the T model). On the other hand, coherent detections are obtained *behind* the main wrap of the trailing arm as predicted by the P model for  $\Lambda \lesssim 240^\circ$ . These detections may indicate a different shape for that portion of the trailing arm. However, as discussed above, they match two more feeble structures running parallel to the main arm. It is obvious that the P model is not adequate to fit all our observations, in spite of the good overall match.
- The most nearby detections are the more difficult to interpret robustly. However the single primary detection at  $d \simeq 13$  kpc and  $\Lambda \simeq 287^\circ$  (just beyond the  $d \leq 12$  kpc “zone of avoidance” of our technique) matches the prediction of all the three L05 models, as well as for the model by Law & Majewski (2010). For this reason we are quite confident to have detected for the first time the nearest wrap

of the leading arm. We are currently following up this finding, to check if the predicted  $d \sim 10$  kpc wrap can be detected also in other *los*.

- The three detections at  $d \sim 20$  kpc and  $\Lambda \simeq 245^\circ$  are matched by a spur of the P model. The two detections at  $d \simeq 18$  kpc and  $\Lambda \gtrsim 260^\circ$  have been tentatively ascribed to the S297+63-20.5/VSS overdensity. The T model matches very well *all* of these detections with a single narrow wrap of the Sgr trailing arm. However Law & Majewski (2010) confirm that the kinematics predicted by their model toward VSS is markedly different from what observed by Duffau et al. (2006) and Newberg et al. (2007).
- The overall trends of FWHM along the *los* as a function of  $\Lambda$  of the P model provide a reasonable match to our primary detections of the leading arm. It is especially interesting to note that the model reproduces the different trends encountered in the two branches, even if it does not produce the observed bifurcation. This seems to provide further support to the view (adopted by Yanny et al. 2009b; Niederste-Ostholt et al. 2010) that branch A and branch B are substructures within the same wrap of the Stream, and not different wraps as proposed by Fellhauer et al. (2006). However, a limited set of tests performed on intra-branches fields suggests that the bifurcation in the Dec direction shown by Belokurov et al. (2006) is real. Probably a deeper, thorough and independent analysis of the Dec structure of this wrap of the Stream is warranted (see Law & Majewski (2010) for possible alternative explanations).
- The observed trends of density as a function of RA along the leading arm (branches A and B) are in fair agreement with those by Niederste-Ostholt et al. (2010). Our estimates of the total luminosity

per kpc at any given RA are lower than theirs by a factor of  $\sim 4 - 5$ .

- Kinematic follow up of the newly identified structures is clearly urgent. Carrell & Wilhelm (2010) recently demonstrated that this can be carried on using exactly the same tracer stars, i.e. RC stars.

This research has been financially supported by INAF through the PRIN 2007 grant CRA 1.06.10.04 “The local route to galaxy formation...” and by ....

This research make use of SDSS data. Funding for the SDSS and SDSS-II has been provided by the Alfred P. Sloan Foundation, the Participating Institutions, the National Science Foundation, the U.S. Department of Energy, the National Aeronautics and Space Administration, the Japanese Monbukagakusho, the Max Planck Society, and the Higher Education Funding Council for England. The SDSS Web Site is <http://www.sdss.org>. The SDSS is managed by the Astrophysical Research Consortium for the Participating Institutions. The Participating Institutions are the American Museum of Natural History, Astrophysical Institute Potsdam, University of Basel, University of Cambridge, Case Western Reserve University, University of Chicago, Drexel University, Fermilab, the Institute for Advanced Study, the Japan Participation Group, Johns Hopkins University, the Joint Institute for Nuclear Astrophysics, the Kavli Institute for Particle Astrophysics and Cosmology, the Korean Scientist Group, the Chinese Academy of Sciences (LAMOST), Los Alamos National Laboratory, the Max-Planck-Institute for Astronomy (MPIA), the Max-Planck-Institute for Astrophysics (MPA), New Mexico State University, Ohio State University, University of Pittsburgh, University of Portsmouth, Princeton University, the United States Naval Observatory, and the University of Washington.

## REFERENCES

Adelman-McCarthy, J. K. et al. 2008, ApJS, 175, 297  
 Alard, C. 1996, ApJ, 458, L17+  
 Alcock, C. et al. 1997, ApJ, 474, 217  
 Babusiaux, C. & Gilmore, G. 2005, MNRAS, 358, 1309  
 Bailin, J. 2003, ApJ, 583, L79  
 Bell, E. F., Zucker, D. B., Belokurov, V., Sharma, S., Johnston, K. V., Bullock, J. S., Hogg, D. W., Jahnke, K., de Jong, J. T. A., Beers, T. C., Evans, N. W., Grebel, E. K., Ivezić, Ž., Koposov, S. E., Rix, H., Schneider, D. P., Steinmetz, M., & Zolotov, A. 2008, ApJ, 680, 295  
 Bellazzini, M., Correnti, M., Ferraro, F. R., Monaco, L., & Montegriffo, P. 2006a, A&A, 446, L1  
 Bellazzini, M., Ferraro, F. R., & Buonanno, R. 1999a, MNRAS, 304, 633  
 —. 1999b, MNRAS, 307, 619  
 Bellazzini, M., Ferraro, F. R., & Ibata, R. 2003a, AJ, 125, 188  
 Bellazzini, M., Gennari, N., & Ferraro, F. R. 2005, MNRAS, 360, 185  
 Bellazzini, M., Ibata, R., Ferraro, F. R., & Testa, V. 2003b, A&A, 405, 577  
 Bellazzini, M., Ibata, R., Martin, N., Lewis, G. F., Conn, B., & Irwin, M. J. 2006b, MNRAS, 366, 865  
 Bellazzini, M., Ibata, R. A., Chapman, S. C., Mackey, A. D., Monaco, L., Irwin, M. J., Martin, N. F., Lewis, G. F., & Dalessandro, E. 2008, AJ, 136, 1147  
 Bellazzini, M., Newberg, H. J., Correnti, M., Ferraro, F. R., & Monaco, L. 2006c, A&A, 457, L21  
 Belokurov, V., Evans, N. W., Irwin, M. J., Lynden-Bell, D., Yanny, B., Vidrih, S., Gilmore, G., Seabroke, G., Zucker, D. B., Wilkinson, M. I., Hewett, P. C., Bramich, D. M., Fellhauer, M., Newberg, H. J., Wyse, R. F. G., Beers, T. C., Bell, E. F., Barentine, J. C., Brinkmann, J., Cole, N., Pan, K., & York, D. G. 2007, ApJ, 658, 337  
 Belokurov, V. et al. 2006, ApJ, 642, L137  
 Bonifacio, P. et al. 2006, in ESO Astrophysics Symposium, Vol. 000, The Milky Way and its Satellites, ed. V. Hill & L. Pasquini, 232–235  
 Bullock, J. S., Kravtsov, A. V., & Weinberg, D. H. 2001, ApJ, 548, 33  
 Carlin, J. L., Grillmair, C. J., Muñoz, R. R., Nidever, D. L., & Majewski, S. R. 2009, ApJ, 702, L9  
 Carrell, K. & Wilhelm, R. 2010, ArXiv e-prints  
 Chou, M.-Y. et al. 2007, ApJ, 670, 346  
 Cole, N. et al. 2008, ApJ, 683, 750  
 Cordier, D., Pietrinferni, A., Cassisi, S., & Salaris, M. 2007, AJ, 133, 468  
 Correnti, M., Bellazzini, M., & Ferraro, F.R., 2007, in Stellar Populations as Building Blocks of Galaxies, A. Vazdekis and R. F. Peletier Eds., Cambridge: Cambridge University Press, IAU Symp., 241, 329  
 Correnti, M., Bellazzini, M., & Ferraro, F.R., 2008, in XXI Century Challenges for Stellar Evolution, S. Cassisi and M. Salaris Eds., Pisa-Roma: Fabrizio Serra, Mem. SAIt., 79, 692

Correnti, M., Bellazzini, M., & Ferraro, F. R. 2009, MNRAS, 397, L26

Cseresnjes, P. 2001, A&A, 375, 909

de Jong, J. T. A., Yanny, B., Rix, H., Dolphin, A. E., Martin, N. F., & Beers, T. C. 2009, ArXiv e-prints

Duffau, S., Zinn, R., Vivas, A. K., Carraro, G., Méndez, R. A., Winnick, R., & Gallart, C. 2006, ApJ, 636, L97

Edelsohn, D. J. & Elmegreen, B. G. 1997, MNRAS, 290, 7

Fahlman, G. G., Mandushev, G., Richer, H. B., Thompson, I. B., & Sivaramakrishnan, A. 1996, ApJ, 459, L65+

Fellhauer, M., Belokurov, V., Evans, N. W., Wilkinson, M. I., Zucker, D. B., Gilmore, G., Irwin, M. J., Bramich, D. M., Vidrih, S., Wyse, R. F. G., Beers, T. C., & Brinkmann, J. 2006, ApJ, 651, 167

Girardi, L. & Salaris, M. 2001, MNRAS, 323, 109

Giuffrida, G., Sbordone, L., Zaggia, S., Marconi, G., Bonifacio, P., Izzo, C., Szeifert, T., & Buonanno, R., 2010, A&A, 513, 62

Gómez-Flechoso, M. A., Fux, R., & Martinet, L. 1999, A&A, 347, 77

Grillmair, C. J. 2009, ApJ, 693, 1118

Grillmair, C. J. & Dionatos, O. 2006, ApJ, 643, L17

Grillmair, C. J. & Johnson, R. 2006, ApJ, 639, L17

Helmi, A. 2004, ApJ, 610, L97

Helmi, A. & White, S. D. M. 2001, MNRAS, 323, 529

Ibata, R., Irwin, M., Lewis, G. F., & Stolte, A. 2001a, ApJ, 547, L133

Ibata, R., Lewis, G. F., Irwin, M., Totten, E., & Quinn, T. 2001b, ApJ, 551, 294

Ibata, R. A., Gilmore, G., & Irwin, M. J. 1994, Nature, 370, 194

—. 1995, MNRAS, 277, 781

Ibata, R. A. & Lewis, G. F. 1998, ApJ, 500, 575

Ibata, R. A., Lewis, G. F., Irwin, M. J., & Cambrésy, L. 2002, MNRAS, 332, 921

Ibata, R. A. & Razoumov, A. O. 1998, A&A, 336, 130

Ibata, R. A., Wyse, R. F. G., Gilmore, G., Irwin, M. J., & Suntzeff, N. B. 1997, AJ, 113, 634

Ivezic, Z., Goldston, J., Finlator, K., Knapp, G. R., Yanny, B., McKay, T. A., Amrose, S., Krisciunas, K., Willman, B., Anderson, S., Schaber, C., Erb, D., Logan, C., Stubbs, C., Chen, B., Nielsen, E., Uomoto, A., Pier, J. R., Fan, X., Gunn, J. E., Lupton, R. H., Rockosi, C. M., Schlegel, D., Strauss, M. A., Annis, J., Brinkmann, J., Csabai, I., Doi, M., Fukugita, M., Hennessy, G. S., Hindsley, R. B., Margon, B., Munn, J. A., Newberg, H. J., Schneider, D. P., Smith, J. A., Szokoly, G. P., Thakar, A. R., Vogeley, M. S., Waddell, P., Yasuda, N., & York, D. G. 2000a, AJ, 120, 963

Ivezic, Z. et al. 2000b, AJ, 120, 963

Jiang, I. & Binney, J. 2000, MNRAS, 314, 468

Johnston, K. V., Law, D. R., & Majewski, S. R. 2005, ApJ, 619, 800

Johnston, K. V., Majewski, S. R., Siegel, M. H., Reid, I. N., & Kunkel, W. E. 1999, AJ, 118, 1719

Johnston, K. V., Spergel, D. N., & Hernquist, L. 1995, ApJ, 451, 598

Jurić, M. et al. 2008, ApJ, 673, 864

Keller, S. C. 2009a, ArXiv e-prints

—. 2009b, ArXiv e-prints

Keller, S. C., da Costa, G. S., & Prior, S. L. 2009, MNRAS, 394, 1045

Keller, S. C., Murphy, S., Prior, S., Da Costa, G., & Schmidt, B. 2008, ApJ, 678, 851

Kunder, A. & Chaboyer, B. 2009, AJ, 137, 4478

Lagadec, E. et al. 2009, MNRAS, 396, 598

Laird, J. B., Carney, B. W., Rupen, M. P., & Latham, D. W. 1988, AJ, 96, 1908

Landolt, A. U. 1992, AJ, 104, 340

Law, D. R., Johnston, K. V., & Majewski, S. R. 2005, ApJ, 619, 807

Law, D. R. & Majewski, S. R. 2010, ArXiv e-prints

Law, D. R., Majewski, S. R., & Johnston, K. V. 2009, ApJ, 703, L67

Layden, A. C. & Sarajedini, A. 2000, AJ, 119, 1760

Madau, P., Kuhlen, M., Diemand, J., Moore, B., Zemp, M., Potter, D., & Stadel, J. 2008, ApJ, 689, L41

Majewski, S. R., Siegel, M. H., Kunkel, W. E., Reid, I. N., Johnston, K. V., Thompson, I. B., Landolt, A. U., & Palma, C. 1999, AJ, 118, 1709

Majewski, S. R., Skrutskie, M. F., Weinberg, M. D., & Ostheimer, J. C. 2003, ApJ, 599, 1082

Majewski, S. R. et al. 2004, AJ, 128, 245

Martin, N. F., Ibata, R. A., Bellazzini, M., Irwin, M. J., Lewis, G. F., & Dehnen, W. 2004, MNRAS, 348, 12

Martínez-Delgado, D., Aparicio, A., Gómez-Flechoso, M. Á., & Carrera, R. 2001, ApJ, 549, L199

Martínez-Delgado, D., Gómez-Flechoso, M. Á., Aparicio, A., & Carrera, R. 2004, ApJ, 601, 242

Martínez-Delgado, D., Peñarrubia, J., Jurić, M., Alfaro, E. J., & Ivezic, Z. 2007, ApJ, 660, 1264

Mateo, M., Kubiak, M., Szymanski, M., Kaluzny, J., Krzeminski, W., & Udalski, A. 1995a, AJ, 110, 1141

Mateo, M., Mirabal, N., Udalski, A., Szymanski, M., Kaluzny, J., Kubiak, M., Krzeminski, W., & Stanek, K. Z. 1996, ApJ, 458, L13+

Mateo, M., Olszewski, E. W., & Morrison, H. L. 1998, ApJ, 508, L55

Mateo, M., Udalski, A., Szymanski, M., Kaluzny, J., Kubiak, M., & Krzeminski, W. 1995b, AJ, 109, 588

Mc William, A. & Smecker-Hane, T. 2006, in ESO Astrophysics Symposium, Vol. 000, The Milky Way and its Satellites, ed. V. Hill & L. Pasquini, 236–239

Monaco, L., Bellazzini, M., Bonifacio, P., Buzzoni, A., Ferraro, F. R., Marconi, G., Sbordone, L., & Zaggia, S. 2007, A&A, 464, 201

Monaco, L., Bellazzini, M., Bonifacio, P., Ferraro, F. R., Marconi, G., Pancino, E., Sbordone, L., & Zaggia, S. 2005a, A&A, 441, 141

Monaco, L., Bellazzini, M., Ferraro, F. R., & Pancino, E. 2003, ApJ, 597, L25

—. 2004, MNRAS, 353, 874

—. 2005b, MNRAS, 356, 1396

Monaco, L., Ferraro, F. R., Bellazzini, M., & Pancino, E. 2002, ApJ, 578, L47

Newberg, H. J., Yanny, B., Cole, N., Beers, T. C., Re Fiorentin, P., Schneider, D. P., & Wilhelm, R. 2007, ApJ, 668, 221

Newberg, H. J. et al. 2002, ApJ, 569, 245

Niederste-Ostholt, M., Belokurov, V., Evans, N. W., & Penarrubia, J. 2010, ArXiv e-prints

Paczynski, B. & Stanek, K. Z. 1998, ApJ, 494, L219+

Peñarrubia, J., Navarro, J. F., & McConnachie, A. W. 2008, ApJ, 673, 226

Pietrinferni, A., Cassisi, S., Salaris, M., & Castelli, F. 2004, ApJ, 612, 168

Prior, S. L., Da Costa, G. S., & Keller, S. C. 2009a, ApJ, 704, 1327

Prior, S. L., Da Costa, G. S., Keller, S. C., & Murphy, S. J. 2009b, ApJ, 691, 306

Renzini, A. 1998, AJ, 115, 2459

Renzini, A. & Buzzoni, A. 1986, in Astrophysics and Space Science Library, Vol. 122, Spectral Evolution of Galaxies, ed. C. Chiosi & A. Renzini, 195–231

Renzini, A. & Fusi Pecci, F. 1988, ARA&A, 26, 199

Robin, A. C., Reylé, C., Derrière, S., & Picaud, S. 2003, A&A, 409, 523

Rockosi, C. M. et al. 2002, AJ, 124, 349

Sbordone, L., Bonifacio, P., Buonanno, R., Marconi, G., Monaco, L., & Zaggia, S. 2007, A&A, 465, 815

Schlegel, D. J., Finkbeiner, D. P., & Davis, M. 1998, ApJ, 500, 525

Seabroke, G. M., Gilmore, G., Siebert, A., Bienaymé, O., Binney, J., Bland-Hawthorn, J., Campbell, R., Freeman, K. C., Gibson, B., Grebel, E. K., Helmi, A., Munari, U., Navarro, J. F., Parker, Q. A., Siviero, A., Steinmetz, M., Watson, F. G., Wyse, R. F. G., Zwitter, T., Peñarrubia, J., Smith, M. C., & Williams, M. 2008, MNRAS, 384, 11

Siegel, M. H., Dotter, A., Majewski, S. R., Sarajedini, A., Chaboyer, B., Nidever, D. L., Anderson, J., Marin-Franch, A., Rosenberg, A., Bedin, L. R., Aparicio, A., King, I., Piotto, G., & Reid, I. N. 2007, ApJ, 667, L57

Skrutskie, M. F. et al. 2006, AJ, 131, 1163

Stanek, K. Z. & Garnavich, P. M. 1998, ApJ, 503, L131+

Stetson, P. B. 2000, PASP, 112, 925

Unavane, M., Wyse, R. F. G., & Gilmore, G. 1996, MNRAS, 278, 727

Velazquez, H. & White, S. D. M. 1995, MNRAS, 275, L23

Vivas, A. K., Jaffé, Y. L., Zinn, R., Winnick, R., Duffau, S., & Mateo, C. 2008, AJ, 136, 1645

Vivas, A. K. & Zinn, R. 2006, AJ, 132, 714

Yanny, B., Newberg, H. J., Johnson, J. A., Lee, Y. S., Beers, T. C., Bizyaev, D., Brewington, H., Fiorentin, P. R., Harding, P., Malanushenko, E., Malanushenko, V., Oravetz, D., Pan, K., Simmons, A., & Snedden, S. 2009a, *ApJ*, 700, 1282

Yanny, B. et al. 2000, *ApJ*, 540, 825

—. 2003, *ApJ*, 588, 824

—. 2009b, *AJ*, 137, 4377